DRAFT VERSION OCTOBER 31, 2025
Typeset using LaTeX **twocolumn** style in AASTeX7

Weak-Lensing Detection of Intercluster Filaments in Three Nearby Cluster Systems

RAHUL SHINDE [1] AND IAN DELL'ANTONIO [1]

[1] *Department of Physics, Brown University, 182 Hope Street, Box 1843, Providence, RI 02912, USA*

(Received October 29, 2025)

Submitted to ApJ

ABSTRACT

Direct detection of intercluster filaments is challenging due to their low surface density, resulting in a weak deflection field. We present weak-lensing detections of intercluster filaments using wide-field Dark Energy Camera (DECam) observations from the Local Volume Complete Cluster Survey (LoVoCCS). A matched-filter method was applied to identify filamentary structures in three nearby ($z < 0.1$) systems centered on Abell 401, Abell 2029, and Abell 3558. We discover two prominent filaments ($\geq 4\sigma$) in each system, with the strongest detections ($6.4\sigma - 7.3\sigma$) around Abell 401 and Abell 2029. In particular, we report the first robust weak-lensing detections ($> 5\sigma$) of the intercluster bridges connecting the cluster pairs Abell 401/399, Abell 2029/2033, Abell 2029/SIG, and Abell 3558/3556. Adopting a filament convergence model motivated by numerical simulations, we infer the maximum convergence (κ_0) and characteristic width ($h_{\rm c}$) for all six filaments, yielding $\kappa_0 \sim 0.015 - 0.053$ and $h_{\rm c} \sim 0.11 - 0.45$ Mpc. The performance of the matched-filter technique is validated using mock shear catalogs and further tested on a null field around Abell 2351. We also explore the potential of using the B-mode lensing signal of filaments to suppress cluster-induced shear contamination. These results demonstrate the feasibility of directly mapping dark matter filaments with current and future wide-field weak-lensing datasets.

Keywords: Weak gravitational lensing (1797) — Galaxy clusters (584) — Abell clusters (9) — Dark matter (353) — Large-scale structure of the universe (902) — Observational cosmology (1146)

1. INTRODUCTION

Predictions from N-body simulations of the standard ΛCDM cosmological model (V. Springel et al. 2005), supported by observational evidence from spectroscopic surveys (M. Colless et al. 2001; D. H. Jones et al. 2009; I. Zehavi et al. 2011), confirm that matter in the universe is organized in a *cosmic web* structure. This hierarchical structure consists of near-empty regions (voids), enclosed by high-density walls (sheets), which intersect to form linear structures (filaments) that transport matter into dense nodes (clusters) (J. R. Bond et al. 1996). Filaments are estimated to contain roughly half of the matter in the universe (M. Cautun et al. 2014). By regulating cluster growth and sustaining galaxy formation, filaments offer a unique avenue to probe structure formation history, constrain the nature of dark matter, and infer properties of the underlying cosmology.

Cosmic filaments have been studied using various complementary probes. X-ray and Sunyaev-Zel'dovich (SZ) observations trace the diffuse baryonic component – the warm hot intergalactic medium (WHIM) – distributed along filaments (N. Werner et al. 2008; F. Radiconi et al. 2022; A. D. Hincks et al. 2022; M. S. Mirakhor et al. 2022; K. Migkas et al. 2025). Spectroscopic redshift surveys, on the other hand, map the spatial distribution of luminous galaxies that outline the filamentary skeleton. However, both approaches have limitations; redshift surveys are limited to bright galaxies and are affected by galaxy bias, whereas X-ray and SZ analyses rely on assumptions about the thermodynamic state of the filamentary gas. As a result, they only provide partial and biased information about the underlying matter distribution. In contrast to baryonic tracers, gravitational lensing offers the most unambiguous way to measure the total projected mass distribution, luminous and dark matter alike, in filaments.

The direct detection of filaments via their lensing signal, however, remains challenging and has only been reported in a small number of cases (J. P. Dietrich et al. 2012; M. Jauzac et al. 2012; K. HyeongHan et al. 2024). The intrinsically low-density contrast of filaments results in a weak deflection field. The signal is dominated by shape noise and further obscured by contamination from neighboring clusters and large-scale structure along the line of sight. Consequently, most studies have focused on inferring ensemble properties of filaments through stacking methods (J. Clampitt et al. 2016; S. D. Epps & M. J. Hudson 2017; H. Kondo et al. 2020; Q. Xia et al. 2020). Robust detection of individual filaments, therefore, requires targeted exploitation of their linear morphology and a rigorous treatment of noise. In this paper, we implement the matched-filter technique introduced in M. Maturi et al. (2005) to detect the presence of filamentary structures in three systems centered on (i) Abell 401, (ii) Abell 2029, and (iii) Abell 3558 (Shapley Supercluster Core).

The remainder of the paper is structured as follows. Section 2 reviews the fundamentals of weak-lensing theory and introduces the filament shear model. Section 3 discusses the challenges associated with detecting filaments via their shear signature and the impact of noise. In Section 4, we present a shear decomposition scheme that leverages filament geometry and motivates a filter-based approach. Section 5 details the construction of the optimal matched filter and examines the impact of noise on our analysis. The efficacy of the matched-filter method is demonstrated in Section 6 using mock data. Here, we also explore the potential of using the B-mode signal for filament detection in conjunction with the E-mode signal. Section 7 describes the LoVoCCS dataset and our results are presented in Section 8. Finally, we summarize our conclusions and outline directions for future work in Section 9.

Throughout this paper, we assume a concordance ΛCDM cosmology with $H_0 = 71\,\mathrm{km\,s^{-1}\,Mpc^{-1}}$ and $\Omega_\mathrm{m} = 0.2648$.

2. WEAK-LENSING FORMALISM

In this section, we provide a brief overview of the weak lensing theory to establish a connection between lensing quantities and observables (for more details, see M. Bartelmann & P. Schneider 2001). We consider the 2-D lensing potential $\psi(\boldsymbol{x})$, corresponding to the surface mass density $\Sigma(\boldsymbol{x})$, under the thin-lens approximation:

$$\psi(\boldsymbol{x}) = \frac{4G}{c^2}\frac{D_\mathrm{l}D_\mathrm{ls}}{D_\mathrm{s}}\int \mathrm{d}^2x'\,\Sigma(\boldsymbol{x}')\ln|\boldsymbol{x}-\boldsymbol{x}'|. \quad (1)$$

Here, D_l, D_s, and D_{ls} denote the angular diameter distances between the observer and lens, the observer and source, and the lens and source, respectively. G is the gravitational constant and c is the speed of light. $\boldsymbol{x} = \{x_1, x_2\}$ represents the Cartesian angular position vector in the plane of the sky. Let (r, ϕ) be the corresponding polar representation.

First-order lensing quantities like the scalar convergence (κ) and complex shear ($\gamma = \gamma_1 + \mathrm{i}\gamma_2$) can be derived using the complex lensing operator $\partial = \frac{\partial}{\partial x_1} + \mathrm{i}\frac{\partial}{\partial x_2}$.

$$\kappa = \frac{\partial\partial^*\psi}{2}, \quad (2)$$

$$\gamma = \frac{\partial\partial\psi}{2}. \quad (3)$$

In practice, we can only measure the reduced shear $g = \gamma/(1-\kappa)$, which, in the weak-lensing limit $\kappa \ll 1$, can be approximated as $g \approx \gamma$. The shear catalog used in this work is derived from the LoVoCCS Survey (S. Fu et al. 2022), which employs the HSM algorithm (C. Hirata & U. Seljak 2003; R. Mandelbaum et al. 2005, 2018) to measure galaxy shapes and obtain reduced shear estimates. The HSM algorithm adopts the *distortion* definition of the complex ellipticity,

$$\chi = \frac{1-q^2}{1+q^2}e^{2\mathrm{i}\phi},$$

where $q = b/a$ is the ratio of the semi-minor axis to the semi-major axis, and ϕ is the position angle of the galaxy. Under a shear, χ transforms from the unlensed intrinsic source ellipticity χ_s as

$$\chi = \frac{\chi_\mathrm{s} + 2g + g^2\chi_\mathrm{s}^*}{1 + |g|^2 + 2\,\mathrm{Re}(g\chi_\mathrm{s}^*)}.$$

In the weak-lensing regime ($\gamma \ll 1$, $\kappa \ll 1$), under the assumption that the source galaxies are randomly oriented, i.e., $\langle\chi_\mathrm{s}\rangle = \langle\chi_\mathrm{s}^2\rangle = 0$, it follows to first order that $\frac{\langle\chi\rangle}{2} \approx g \approx \gamma$. Thus, the observed image ellipticity provides an unbiased, albeit noisy, estimate of the local shear. Henceforth, we drop the distinction between the true shear and the observed shear estimate, using γ to denote both and σ_γ for the corresponding uncertainty.

2.1. *Shear Model*

We can now proceed to evaluate the lensing quantities described above for typical cluster–filament configurations. In this work, we study a mass model consisting of an isotropic central cluster (primary) with radially emanating filament(s). We also include possible contamination from neighboring isotropic clusters (secondary). For simplicity, we make the following assumptions:

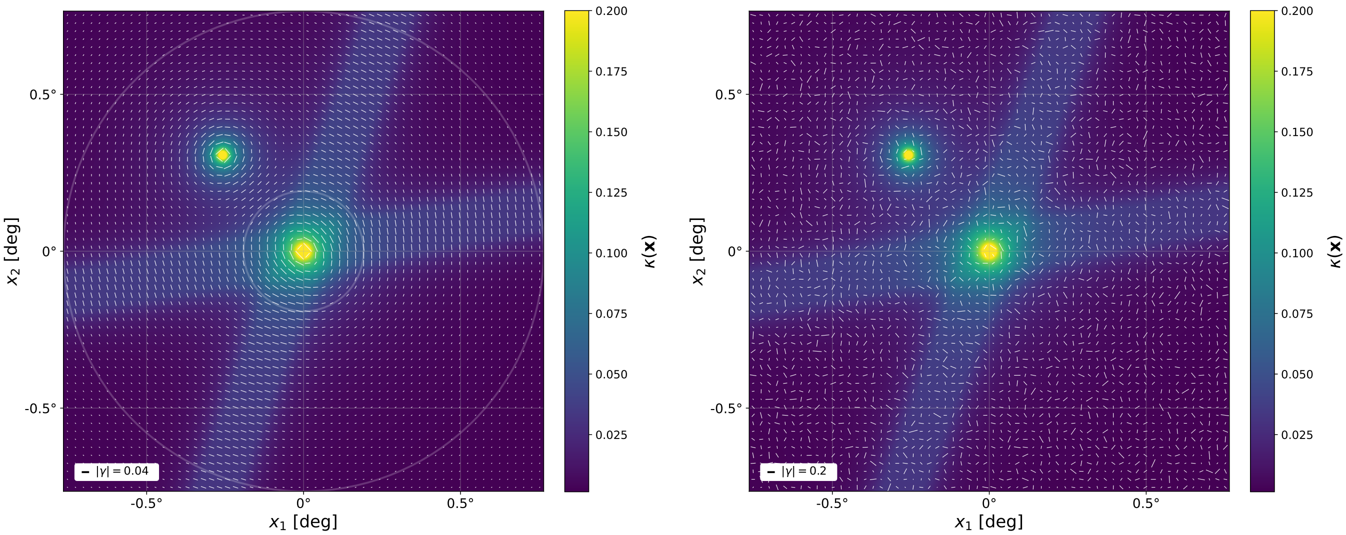

(a) Without Shape Noise

(b) With Shape Noise

Figure 1. Convergence field, $\kappa(\boldsymbol{x})$, and binned shear pattern, $\langle\gamma(\boldsymbol{x})\rangle_{\Delta x}$, for the mock catalog. *Left:* Convergence map of the mock model overlaid with the binned shear pattern, computed using a pixel size of $\Delta x = 1.53$ arcmin. White circles indicate the radial cutoffs ($r_1 = 0.91$ Mpc, $r_2 = 3.64$ Mpc) used to restrict the filter. The legend in the bottom-left corner provides a mapping between the shear length in the plot to the physical shear value. *Right:* Same as left panel, but with shape noise ($\sigma_\gamma = 0.45$) added to the mock shear field. In both panels, convergence values are truncated at $\kappa < 0.2$ to emphasize filamentary structures.

1. Each filament lies in the plane of the sky and extends infinitely away from the central cluster

2. Far removed from adjacent clusters, the filament surface density remains constant along its axis and varies only in the orthogonal direction.

3. The entire system of clusters and filaments is assumed to lie at the same redshift as the primary cluster

Given the limited sky coverage of each system studied in this work ($< 2°$), we adopt the flat-sky approximation and place the origin of the Cartesian coordinate system at the primary cluster, typically the most massive cluster in the field. This choice is motivated by the empirical findings that (1) the surface mass density of a filament increases towards the host cluster, and (2) massive clusters are connected to a greater number of filaments than their less massive counterparts (J. R. Bond et al. 1996; J. M. Colberg et al. 2005; M. Cautun et al. 2014).

From assumption (2) and equations (1), (2), and (3), it follows that, relative to the filament axis, the shear is purely orthogonal; that is, $\gamma_{\mathrm{f},1'} =$ - κ and $\gamma_{\mathrm{f},2'} = 0$, where the primed axes $(1', 2')$ denote the rotated frame aligned with the filament. If the filament subtends a counterclockwise angle θ_f with the positive x_1 axis, we can decompose the shears in the original frame to get

$$\gamma_{\mathrm{f},1} = -\kappa(h)\cos(2\theta_\mathrm{f}),$$
$$\gamma_{\mathrm{f},2} = -\kappa(h)\sin(2\theta_\mathrm{f}),$$

where h is the perpendicular distance from the filament axis.

J. M. Colberg et al. (2005) examined the density profiles of straight filaments in N-body simulations and found that they exhibit well-defined edges, described by the characteristic width h_c, within which the density remains approximately constant. Beyond this edge, the density falls off as h^{-2}. Motivated by this behavior, we adopt the following model for the filament convergence:

$$\kappa(h) = \begin{cases} \kappa_0, & \text{if } h \le h_\mathrm{c}, \\ \dfrac{\kappa_0}{1 + \left(\dfrac{h - h_\mathrm{c}}{h_\mathrm{c}}\right)^2}, & \text{if } h > h_\mathrm{c}. \end{cases} \tag{4}$$

where κ_0 is the maximum convergence at the filament axis. While our model is similar to that implemented in J. M. G. Mead et al. (2010) and K. HyeongHan et al. (2024), we introduce a piecewise function to better capture the flat-top morphology of filaments. However, because of the limited angular resolution of the optimal matched filter (see Figure 3), switching between these model choices has a negligible impact on our results (ΔS/N ≤ 0.01).

We model clusters in the field as spherically symmetric NFW halos (J. F. Navarro et al. 1997), which produce a purely tangential shear relative to the radial direction at each point (r, ϕ). Denoting the radial profile of the cluster shear amplitude by $\gamma_{\rm NFW}(r)$, the cluster shear components in the original frame can be expressed as

$$\gamma_{\rm c,1}(r,\phi) = -\gamma_{\rm NFW}(r)\cos(2\phi),$$
$$\gamma_{\rm c,2}(r,\phi) = -\gamma_{\rm NFW}(r)\sin(2\phi).$$

Figure 1(a) illustrates the shear pattern of an example field comprising a primary cluster, two filaments, and a secondary cluster.

3. CHALLENGES

The low-density contrast of filaments results in a weak shear field that is difficult to distinguish from the shear field induced by adjacent host clusters. Simulations show that the shear value decreases from $\sim 0.05 - 0.2$ in the outskirts of adjacent clusters to $\sim 0.01 - 0.02$ along the bulk of the filament (K. Dolag et al. 2006). For low-redshift clusters ($z \lesssim 0.1$) in the mass range $10^{14}\,{\rm M}_\odot - 10^{15}\,{\rm M}_\odot$, the cluster-induced shear can reach $\sim 0.005 - 0.01$ even at projected separations comparable to $R_{\rm 200c}$. The filament signal is further obscured by various sources of shear noise. N-body simulations by Y. Higuchi et al. (2014) show that only 4% of intercluster filaments are detectable with a lensing signal-to-noise ratio S/N ≥ 2 under ideal conditions (source density $n_{\rm g} \sim 30$ arcmin^{-2}). Thus, an effective detection strategy necessitates a filter capable of excluding shear contamination from the central and secondary clusters while adequately suppressing noise.

3.1. *Noise*

We account for two primary sources of shear noise in our analysis. The first is shape noise, arising from the intrinsic ellipticity of source galaxies as well as their finite number density. The intrinsic ellipticity contribution can be modeled as Poisson noise with the flat power spectrum, $P_{\rm g}(k) = \sigma_\gamma^2/2n_{\rm g}$. The finite sampling of galaxies, on the other hand, imposes a constraint on the smallest spatial scales that can be reliably probed (see Section 5.2.1). Second, we consider lensing contamination from uncorrelated large-scale structure (LSS) along the line of sight (LOS). H. Hoekstra (2001) showed that distant LSS does not bias mass measurements and can be treated as an additional source of noise. We quantify this effect in the context of our survey in Section 5.2.2. Thus, the total shear noise, $\gamma_{\rm n}(\boldsymbol{x}) = \gamma_{\rm g}(\boldsymbol{x}) + \gamma_{\rm LSS}(\boldsymbol{x})$, can be modeled as a zero-mean isotropic Gaussian field.

4. DATA MODEL

Under the weak-lensing approximation ($\kappa \ll 1$), the linearity of the lensing potential $\psi(\boldsymbol{x})$, together with Eq. (3), implies that the observed shear at any point $\boldsymbol{x}$ in the field can be approximated as the sum of the individual shear components. Therefore, the observed shear $\gamma(\boldsymbol{x})$ can be written as

$$\gamma(\boldsymbol{x}) = \gamma_{\rm c}(\boldsymbol{x}) + \gamma_{\rm f}(\boldsymbol{x}) + \gamma_{\rm n}(\boldsymbol{x}).$$

Or in terms of the tangential and cross components,

$$\gamma_{(+,\times)}(\boldsymbol{x}) = \gamma_{{\rm c},(+,\times)}(\boldsymbol{x}) + \gamma_{{\rm f},(+,\times)}(\boldsymbol{x}) + \gamma_{{\rm n},(+,\times)}(\boldsymbol{x}).$$

4.1. *Shear Decomposition*

Given that filaments exhibit a purely tangential shear profile relative to their axes, we are motivated to examine how the tangential and cross shear components of both filaments and clusters vary when decomposed along different directions. We emphasize that, throughout the paper, "tangential" and "cross" labels denote components defined with respect to the chosen reference frame or direction (e.g., the filament axis), not relative to the radial direction at each point.

Consider a frame obtained by rotating the original frame counterclockwise (CCW) by an angle θ, as shown in Figure 2. The filament shear components, decomposed in the rotated frame, can then be written as

$$\gamma_{\rm f,+}(r,\phi;\theta) = \kappa(h)\cos(2(\theta_{\rm f} - \theta)),$$
$$\gamma_{\rm f,\times}(r,\phi;\theta) = \kappa(h)\sin(2(\theta_{\rm f} - \theta)),$$

where $h = r|\sin(\phi - \theta_{\rm f})|$. Similarly, the cluster shear components in the rotated frame are

$$\gamma_{\rm c,+}(r,\phi;\theta) = \gamma_{\rm NFW}(r)\cos(2(\phi - \theta)),$$
$$\gamma_{\rm c,\times}(r,\phi;\theta) = \gamma_{\rm NFW}(r)\sin(2(\phi - \theta)).$$

Hereafter, we suppress the explicit spatial arguments (r, ϕ) and denote the tangential and cross shear fields relative to the rotated frame as $\gamma_+(\theta)$ and $\gamma_\times(\theta)$.

The animations[2] in R. Shinde et al. (2025) illustrate this decomposition scheme for a system consisting of two filaments and two clusters. The decomposed tangential shear for filaments $\gamma_{\rm f,+}(\theta)$ reaches a maximum when the decomposition axis (θ) is aligned with the filament axis $\theta_{\rm f}$, and vanishes when they are separated by 45°. This behavior motivates the use of the observed tangential shear $\gamma_+(\theta)$, as a diagnostic for identifying filamentary structures.

[2] Available at https://aas245-aas.ipostersessions.com

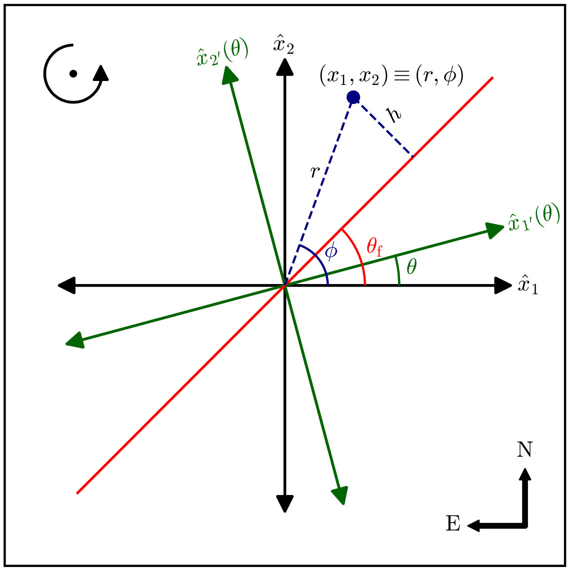

Figure 2. Schematic of the coordinate system and reference frames used in this work. The original frame (black) $\hat{x}_1$–$\hat{x}_2$ is centered on the primary cluster. The decomposition axis or rotated frame (green) $\hat{x}_{1'}$–$\hat{x}_{2'}$ subtends a CCW angle θ with the positive $\hat{x}_1$ axis. The filament (red) is oriented at angle $\theta_{\rm f}$. Any point in the field (blue) can be represented by its Cartesian angular position $\boldsymbol{x} = \{x_1, x_2\}$ or corresponding polar coordinates (r, ϕ). The perpendicular distance of the point from the filament axis is marked by $h = r|\sin(\phi - \theta_{\rm f})|$. The entire coordinate system is right-handed. The compass in the lower-right corner provides the cardinal directions in the image frame.

On the contrary, the decomposed tangential shear for clusters, $\gamma_{{\rm c},+}(\theta)$, exhibits a quadrupolar pattern with four alternating lobes that rotate in phase with the decomposition axis (θ). Consequently, the central cluster produces no directional signal, contributing only a positive bias. The secondary cluster, however, can locally resemble a filament. In Section 6.4 we present a method to break this degeneracy.

5. METHOD

We use the decomposition scheme described in the previous section, along with a filter-based approach to extract the lensing signature of any radially emanating filamentary structures present in the field. To this end, we introduce an optimal matched filter designed to exploit the characteristic geometry of filaments and their influence on local shear patterns, while simultaneously suppressing contamination from surrounding halos and other sources of noise. We follow the recipe first described in M. Maturi & J. Merten (2013) and recently applied to the Coma cluster field by K. HyeongHan et al. (2024) to construct a matched-filter statistic that probes the presence of filaments in all directions.

5.1. *Optimal Matched Filter*

An optimal matched filter refers to a kernel function that guarantees the highest possible signal-to-noise ratio (S/N) when correlated with the signal. Effective filter design requires careful consideration of both the signal shape and the spectral characteristics of the underlying noise.

We use the discretized form of the matched-filter statistics provided by M. Maturi & J. Merten (2013), but adopt the normalization of K. HyeongHan et al. (2024).

$$\Gamma_+(\theta) = \frac{1}{\sum_i \Psi_i} \sum_i \gamma_{+,i}\, \Psi_i, \tag{5}$$

$$\Gamma_\times(\theta) = \frac{1}{\sum_i \Psi_i} \sum_i \gamma_{\times,i}\, \Psi_i, \tag{6}$$

where, $\gamma_{+,i}$ and $\gamma_{\times,i}$ are the tangential and cross components of the complex shear γ_i measured for the i-th galaxy in the field, decomposed along the θ direction. Ψ_i is the value of the filter corresponding to the search angle θ, defined at the position of the i-th galaxy: $\Psi_i(\boldsymbol{x}_i;\theta)$.

We use the expression for the variance of an optimal filter provided in M. Schirmer (2004) and implement the following form for the tangential and cross statistics:

$$\sigma^2_{+,\times}(\theta) = \frac{1}{2(\sum_i \Psi_i)^2} \sum_i |\gamma_i|^2\ \Psi_i^2, \tag{7}$$
$$\text{where } |\gamma_i|^2 = \gamma^2_{+,i} + \gamma^2_{\times,i}.$$

M. Maturi et al. (2005) demonstrated that the optimal filter can be conveniently derived in Fourier space, where it is proportional to the signal shape and inversely weighted by the noise power spectrum. Following this approach, we define the filter in real space to match the tangential shear profile of a filament aligned with it:

$$\tau(\boldsymbol{x}) = \gamma_{f,+}(\boldsymbol{x}; \theta_{\rm f} = \theta) = \kappa(h),$$

and suppress the noise to obtain the optimized filter in Fourier space:

$$\hat{\Psi}(\boldsymbol{k}) = \frac{\hat{\tau}(\boldsymbol{k})}{P_{\rm n}(\boldsymbol{k})}, \tag{8}$$

$$\text{where } \hat{\tau}(\boldsymbol{k}) = \mathcal{F}\{\tau(\boldsymbol{x})\}.$$

Finally, the optimized filter can be expressed in real space through the inverse Fourier transform as

$$\Psi(\boldsymbol{x}) = \mathcal{F}^{-1}\{\hat{\Psi}(\boldsymbol{k})\}. \tag{9}$$

5.2. *Noise Power Spectrum*

As mentioned in Section 3.1, we consider two sources of shear noise — (1) shape noise and (2) LSS noise. The total noise can be modeled as an isotropic Gaussian random field with zero mean, described by the power spectrum

$$P_{\rm n}(k) = P_{\rm g}(k) + P_{\rm LSS}(k).$$

5.2.1. *Shape Noise*

For the shape noise, M. Maturi & J. Merten (2013) use a k-dependent exponential correction to the flat power spectrum given by

$$P_{\rm g}(k) = \frac{\sigma_\gamma^2}{2n_{\rm g}} \exp(\frac{k^2}{n_{\rm g} \ln 2}), \tag{10}$$

which accounts for the average separation of background galaxies. This effectively limits the angular resolution achieved by the filter in real space. The exponential term arises from modeling the low-pass filtering effect of finite sampling as a Gaussian frequency response, $\hat{W}(k) = \exp(-\frac{k^2}{k_{\rm cut}^2})$, with $k_{\rm cut} = \sqrt{n_g \ln 2}$ (M. Maturi et al. 2010). Multiplying this response with the filter in Fourier space yields the effective filter: $\hat{\Psi}(\boldsymbol{k}) = \hat{\tau}(\boldsymbol{k}) \cdot \hat{W}(k)$. Note that the flat term $\frac{\sigma_\gamma^2}{2n_{\rm g}}$ in the noise power spectrum has no impact on the effective filter. In our analysis, we find that Eq. (10) does not adequately capture the excess noise power at low k-modes (or large angular scales), which leads to a suboptimal filter. To address this, we rely on mock data to calibrate the filter (see Appendix A). We generate multiple realizations of signal–plus–noise shear fields that closely mimic the statistical properties of our observations ($\sigma_\gamma = 0.45$) and use them to determine the optimal cutoff frequency that maximizes S/N. As illustrated in Figure 15(a), a cutoff frequency of $k_{\rm cut} \sim \frac{\sqrt{n_{\rm g} \ln 2}}{10} = 0.21$ arcmin^{-1} provides the optimal filter for our dataset, yielding an improvement of ΔS/N ~ 1 over $k_{\rm cut} = \sqrt{n_g \ln 2}$.

5.2.2. *LSS Noise*

To estimate the uncertainty contributed by LSS, we follow the procedure outlined in K. HyeongHan et al. (2024). We use mock weak-lensing maps from the kappaTNG dataset[3] (K. Osato et al. 2021), constructed from IllustrisTNG (TNG300-1) simulations (D. Nelson et al. 2018a; F. Marinacci et al. 2018; J. P. Naiman et al. 2018; D. Nelson et al. 2018b; A. Pillepich et al. 2018). We select shear datasets with a source redshift of $z_{\rm s} = 0.5064$, corresponding to the average effective source redshift in our data, derived from photometric estimates, $\langle z_{\rm eff} \rangle = 0.51$. Here, $z_{\rm eff}$ denotes the source redshift that yields the same lensing efficiency[4] as the entire source population. The κTNG maps span a $5° \times 5°$ field with a resolution of 1024×1024 pixels, yielding a pixel scale of 0.29 arcmin/pixel. This is roughly four times larger than the pixel scale used to bin individual galaxies in our analysis. Instead of interpolating the κTNG maps to obtain shear values at galaxy positions in our survey, we compare the LSS-induced uncertainty directly to the average shape noise in our data binned at the κTNG pixel scale.

To this end, we divide each κTNG field into 9 patches to match the average field of view ($1.5° \times 1.5°$) of the images used in our analysis. We apply the matched-filter described in Section 6.2 to a total of $50 \times 9 = 450$ such patches to estimate the mean standard deviation of the tangential statistic across all angles. On average, we find that the LSS noise contribution ($\langle \sigma_{\rm LSS} \rangle = 0.0001$) is about 20 times smaller than the input shape noise contribution ($\langle \sigma_{\rm shape} \rangle \approx 0.002$), implying that we can safely ignore LSS noise in our analysis. To account for the uncertainty in the photometric redshift estimates, we repeat the analysis using a higher source redshift of $z_{\rm s} = 1.034$, and still find the noise contribution from LSS to be insignificant. Our conclusion differs from that of K. HyeongHan et al. (2024) due to the relatively low source density in our survey ($n_g \approx 7 - 12$ arcmin^{-2}), which results in higher effective shape noise, rendering the LSS noise negligible in comparison.

6. IMPLEMENTATION

6.1. *Mock Catalog*

In this section, we demonstrate the efficacy of the matched-filter method described above using mock data. We generate a mock shear catalog for a cluster–filament configuration closely resembling the system described in K. HyeongHan et al. (2024), placed at redshift $z = 0.07$ (typical of cluster pairs studied in this work). We consider a primary central cluster ($M_{\rm 200c} = 8 \times 10^{14}\,{\rm M}_\odot$) and two identical filaments intersecting the primary cluster at angles $\theta_{\rm f_1} = 10°$ and $\theta_{\rm f_2} = 70°$. We model the filaments using Eq. (4) and set $\kappa_0 = 0.03$ and $h_{\rm c} = 0.25$ Mpc. A secondary cluster, identical to the primary, is placed at $\phi = 130°$ and $r = 1.90$ Mpc (or 24 arcmin) away to serve as a contaminant. We use the lensing engine `galsim.NFWHalo` (B. T. P. Rowe et al. 2015) to compute shear contributions from the primary

[3] https://columbialensing.github.io/

[4] The effective lensing efficiency $\langle \beta \rangle = \int_{z_1}^{\infty} p(z_{\rm s}) \frac{D_{\rm ls}(z_1, z_{\rm s})}{D_{\rm s}(z_{\rm s})}\, dz_{\rm s}$, where $p(z_{\rm s})$ is the normalized distribution of source redshifts.

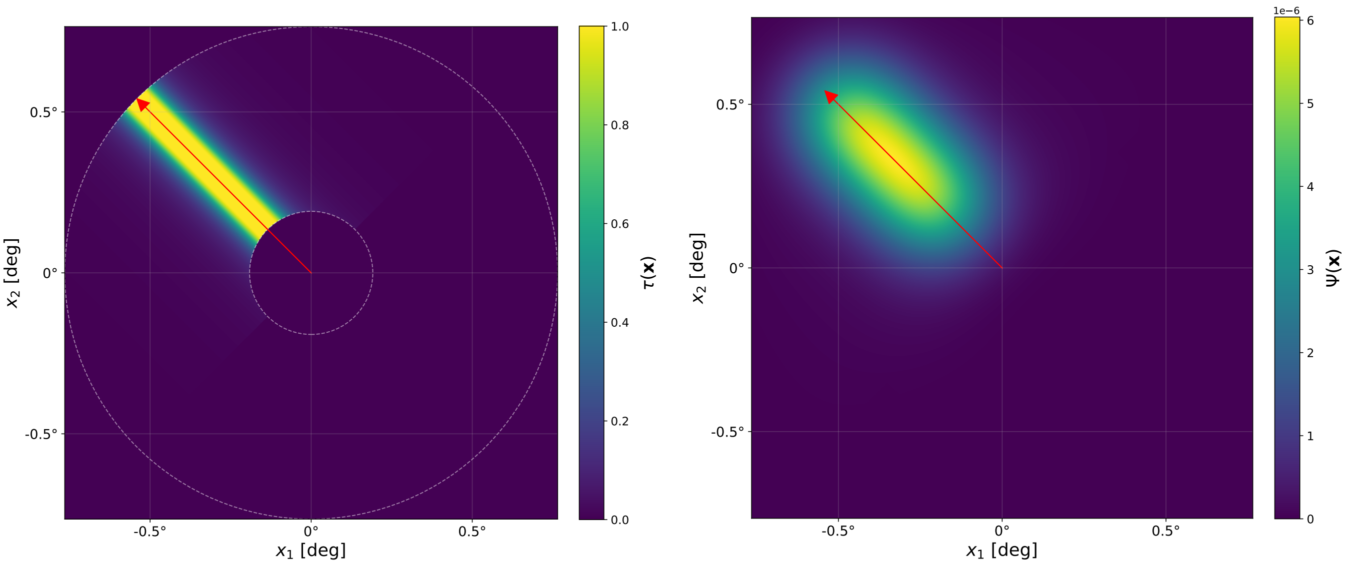

(a) Filter

(b) Optimal Filter

Figure 3. Constructed matched filter and optimal matched filter in real space. *Left:* Matched filter modeled after a template filament with characteristic width $h_{\mathrm{c,filter}} = 0.15$ Mpc and normalization $\kappa_0 = 1$. We note that the choice of κ_0 does not affect the analysis. White dashed circles indicate the radial cutoffs ($r_1 = 0.91$ Mpc, $r_2 = 3.64$ Mpc), and the red arrow marks the filter orientation ($\theta = 135°$). *Right:* Corresponding filter optimized using $\hat{W}(k)$ with a cutoff frequency of $k_{\mathrm{cut}} = 0.21$ arcmin^{-1}.

and secondary clusters. To mimic our observations, we adopt a background source density of $n_g = 8$ arcmin^{-2}. Because our data is largely dominated by the shape noise, we model the total shear noise as a Gaussian field with zero mean and $\sigma_\gamma = 0.45$, consistent with our dataset. Figure 1 illustrates the convergence field and the resulting shear pattern, both with and without noise. To improve interpretability, we display the shear field binned using a grid with pixel size $\Delta x = 1.53$ arcmin. This binning scheme is applied solely for visualization; all analyses reported in this paper use the unbinned shear catalog.

6.2. *Filter*

To construct the unoptimized filter (prior to noise suppression via $\hat{W}(k)$) that follows the filament template, we assume a characteristic width, h_{c}, which represents the typical transverse scale of the filaments of interest. In this work, we use a filter with $h_{\mathrm{c,filter}} = 0.15$ Mpc. Varying the filter width within the range 0.05 Mpc $< h_{\mathrm{c,filter}} <$ 0.25 Mpc changes the resulting S/N only marginally by $\lesssim 3\%$. To minimize shear contamination from both the primary and secondary clusters, we impose radial cutoffs r_1 and r_2, restricting the filter to the annulus $r_1 < r < r_2$. In practice, these cutoffs are chosen such that the cluster shear contribution within the search space remains below 2% (see Appendix B). For the mock run, however, we explicitly include the secondary cluster and set $r_1 = 0.91$ Mpc (11.5 arcmin) and $r_2 = 3.64$ Mpc (46 arcmin) to study its effect on the results. The final parameter that fully specifies the filter is the search angle θ, which defines the orientation of the filter.

The filter can then be optimized in Fourier space according to Eq. (8), and reconstructed in real space via the inverse Fourier transform given in Eq. (9). Since the window function $\hat{W}(k)$ decays exponentially at high frequencies, the optimization process suppresses Fourier modes at the smallest scales. The result is a smoothed filter with limited angular resolution, as illustrated in Figure 3. Once constructed, the optimal matched filter can be convolved with the tangential and cross shear fields to scan all directions θ for the presence of filaments according to Eq. (5) and Eq. (6).

6.3. *Results*

The results for the mock catalog, both with and without noise, are displayed in Figure 4. Since the tangential statistic is expected to vanish in the presence of pure noise ($\langle \Gamma_+(\theta) \rangle_{\mathrm{noise}} = 0$), the significance of each detection is quantified by the signal-to-noise ratio $\mathrm{S/N} = \Gamma_+/\sigma_+$. As expected, the tangential statistic $\Gamma_+(\theta)$ peaks within 3° of the true filament orientations with significance $> 5\sigma$ (see Table 1). Additionally, a lower-significance (3σ) peak is detected in the direction of the secondary cluster, resulting from the tangential

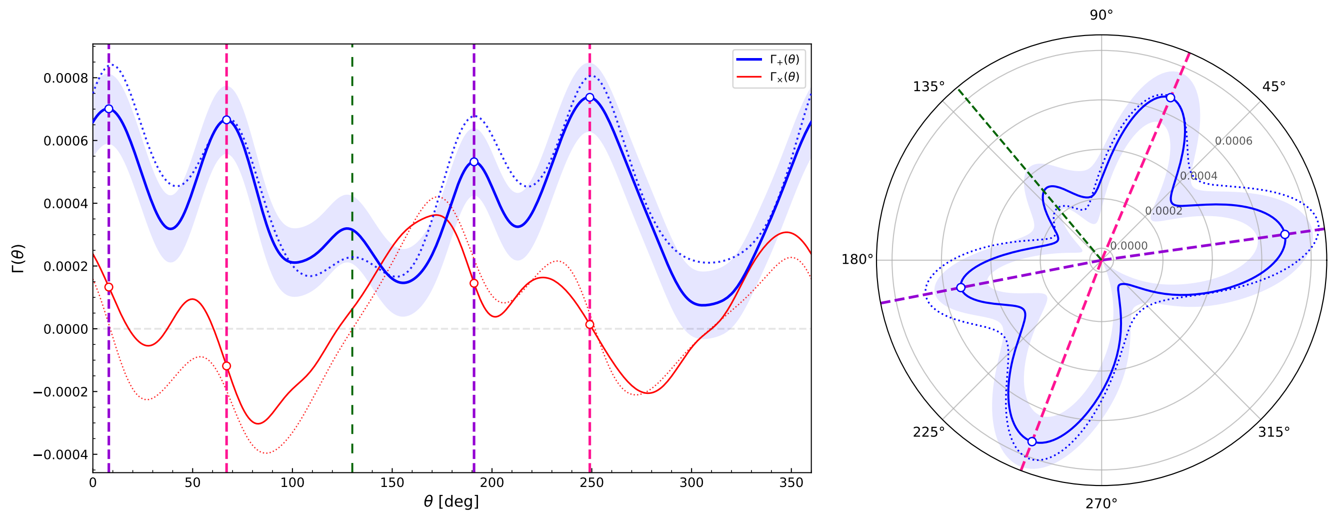

Figure 4. Filament detection results for the mock catalog. *Left:* Matched-filter statistics $\Gamma_\times(\theta)$ and $\Gamma_+(\theta)$ as a function of the search angle θ. The blue and red solid lines correspond to the tangential and cross components, respectively, with the light blue shade indicating the 1σ uncertainty in the tangential signal. The uncertainty in the cross signal is omitted for visual clarity. The dotted blue and red lines denote the corresponding statistics in the absence of noise. The violet and pink vertical dashed lines represent detections associated with filaments oriented at $\theta_{\mathrm{f}_1} = 10^\circ$ and $\theta_{\mathrm{f}_2} = 70^\circ$, respectively ; the green dashed line marks the orientation of the secondary cluster ($\phi = 130^\circ$). *Right:* Polar representation of the left panel

Table 1. Filament Properties - Mock Catalog

Filament Orientation (deg)	Detected Orientation (deg)	Peak Significance (σ)	κ_0	h_{c} (Mpc)
10	8	6.4	$0.034^{+0.006}_{-0.006}$	$0.29^{+0.06}_{-0.05}$
70	67	6.3	$0.029^{+0.007}_{-0.006}$	$0.27^{+0.06}_{-0.05}$
190	191	5.1	$0.030^{+0.008}_{-0.007}$	$0.21^{+0.05}_{-0.05}$
250	249	6.8	$0.032^{+0.006}_{-0.006}$	$0.33^{+0.08}_{-0.06}$

alignment of the cluster shear along the filter axis. This implies that the presence of a secondary cluster in the field can lead to a spurious filament detection. To validate our results, we perform the analysis on 10 realizations of pure-noise shear fields and find no peaks with significance greater than 2σ, indicating that the $\gtrsim 2\sigma$ peaks observed in signal-plus-noise runs are unlikely to be noise-induced artifacts. In the next section, we discuss a strategy to eliminate false positives arising from cluster contamination.

6.4. *Combined Statistic*

A key observation that resolves the cluster-filament degeneracy is that the cross statistic exhibits a sharp decline in the immediate vicinity of the filament axis, while no such behavior is seen for the secondary cluster. This distinction becomes more evident when the negative gradient of the cross statistic (negative cross gradient hereafter) is plotted alongside the tangential statistic as shown in Figure 5. This motivates a closer inspection of the negative cross gradient, $-\partial_\theta \Gamma_\times(\theta)$, to glean additional information that, in conjunction with the tangential statistic, can help distinguish cluster contribution from genuine filament signal.

For the i-th galaxy, the tangential and cross shear components are defined as

$$\gamma_{+,i}(\theta) = -\gamma_{1,i}\cos(2\theta) - \gamma_{2,i}\sin(2\theta),$$

$$\gamma_{\times,i}(\theta) = \quad \gamma_{1,i}\sin(2\theta) - \gamma_{2,i}\cos(2\theta).$$

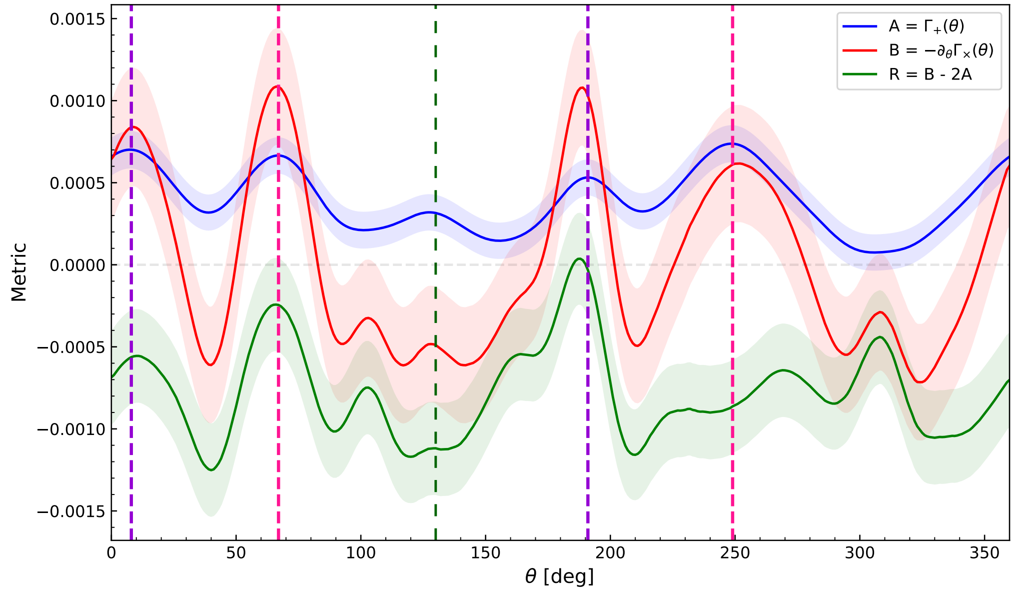

Figure 5. Orthogonal decomposition of the negative cross gradient. The blue, red and green solid lines represent the tangential statistic, $A(\theta)$, negative cross gradient, $B(\theta)$, and the residual, $R(\theta)$. The corresponding shaded regions represent the 1σ uncertainty in each statistic.

Rewriting Eqs. (5) and (6) in terms of the normalized filter function $\tilde{\Psi}_i = \frac{\Psi_i}{\sum_i \Psi_i}$, we obtain

$$\Gamma_+(\theta) = \sum_i \tilde{\Psi}_i(\theta)\,\gamma_{+,i}(\theta),$$
$$\Gamma_\times(\theta) = \sum_i \tilde{\Psi}_i(\theta)\,\gamma_{\times,i}(\theta).$$

For ease of notation, we define the statistics

$$A(\theta) = \Gamma_+(\theta),$$
$$B(\theta) = -\partial_\theta \Gamma_\times(\theta).$$

Differentiating $\Gamma_\times(\theta)$ with respect to θ gives

$$\frac{\partial}{\partial\theta}\Gamma_\times(\theta) = \sum_i \frac{\partial\tilde{\Psi}_i(\theta)}{\partial\theta}\,\gamma_{\times,i}(\theta) + \sum_i \tilde{\Psi}_i(\theta)\,\frac{\partial\gamma_{\times,i}(\theta)}{\partial\theta}. \tag{11}$$

The derivative of $\gamma_{\times,i}(\theta)$ with respect to θ is

$$\frac{\partial\gamma_{\times,i}}{\partial\theta} = 2\,\gamma_{1,i}\cos(2\theta) + 2\,\gamma_{2,i}\sin(2\theta) = -2\,\gamma_{+,i}(\theta). \tag{12}$$

Substituting Eq. (12) into Eq. (11) yields

$$\partial_\theta\Gamma_\times(\theta) = \sum_i \frac{\partial\tilde{\Psi}_i}{\partial\theta}\,\gamma_{\times,i}(\theta) - \ 2\underbrace{\sum_i \tilde{\Psi}_i(\theta)\,\gamma_{+,i}(\theta)}_{A(\theta)}.$$

Thus, we obtain

$$B(\theta) = 2\,A(\theta)\ -\ \sum_i \frac{\partial\tilde{\Psi}_i}{\partial\theta}\,\gamma_{\times,i}(\theta),$$

or equivalently, the compact identity

$$\boxed{B = 2A + R},$$

where the residual term is defined as

$$R(\theta) =\ -\sum_i \frac{\partial\tilde{\Psi}_i}{\partial\theta}\,\gamma_{\times,i}(\theta).$$

Since the normalization factor $\sum_i \Psi_i$ does not vary with the search angle θ, i.e. $\partial_\theta(\sum_i \Psi_i) = 0$, the variance of the residual can be written, analogous to Eq. (7), as

$$\sigma_R^2 = \frac{1}{2}\sum_i (\partial_\theta\tilde{\Psi}_i)^2\,|\gamma_i|^2.$$

Finally, the covariance between A and R is given by

$$\mathrm{Cov}(A,R) = -\sum_i \tilde{\Psi}_i(\theta)\frac{\partial\tilde{\Psi}_i(\theta)}{\partial\theta}\mathrm{Cov}(\gamma_{+,i},\gamma_{\times,i}).$$

Under the assumption of isotropic noise, $\mathrm{Cov}(\gamma_{+,i},\gamma_{\times,i}) = 0$, and consequently, $\mathrm{Cov}(A,R) = 0$. This implies that the tangential statistic A and the residual R are independent metrics that together form an orthogonal basis for representing the negative cross gradient B. Within this basis, the decomposition $B = 2A + R$ highlights that, although B is strongly

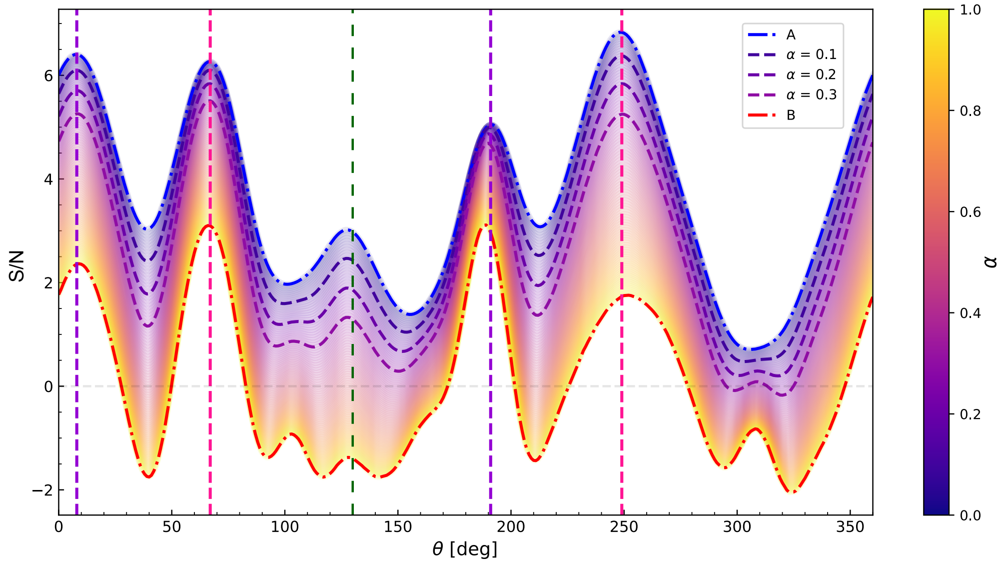

Figure 6. Signal-to-noise ratio (S/N) for linear combinations of the tangential statistic, $A(\theta)$, and the residual, $R(\theta)$. The free parameter $\alpha \in [0, 1]$ is mapped according to the color bar. The corresponding locus of S/N curves representing the combined statistic $L(\alpha) = 2A + \alpha R$ is shown. Three dashed S/N(α) curves corresponding to $\alpha = \{0.1,\ 0.2,\ 0.3\}$ illustrate the effect of progressively adding the residual term to the tangential statistic. The blue and red dash-dot curves represent the extremes, $\alpha = 0$ or $A(\theta)$, and $\alpha = 1$ or $B(\theta)$, respectively.

correlated with A, it is precisely the contribution of R in B that enables the distinction between the filament signature and cluster contamination.

To determine the optimal contribution of R that maximizes the detection S/N, we introduce the combined statistic

$$L(\alpha) = 2A + \alpha R,$$

where α is a free parameter that can be tuned to optimize L. Setting $\alpha = 0$ recovers the tangential statistic A, while $\alpha = 1$ corresponds to the negative cross gradient B. Since both means vanish under noise, i.e., $\langle A\rangle_{\rm noise} = \langle R\rangle_{\rm noise} = 0$, the S/N can be written as

$$\mathrm{S/N}(\alpha) = \frac{2A + \alpha R}{\sqrt{4\sigma_A^2 + \alpha^2\sigma_R^2}}.$$

We find that the residual is inherently more sensitive to noise than the tangential statistic ($\sigma_R \gg \sigma_A$). As a result, introducing a residual-weighted term to the tangential statistic ($\alpha > 0$) does not generally improve the S/N for filament detections. For small values of alpha ($\alpha \sim 0.1 - 0.3$), the combined statistic partially suppresses contamination from the secondary cluster – reducing its significance from $\sim 3\sigma$ to $\sim 1\sigma$ – while maintaining S/N > 5 at all filament peaks. As $\alpha \to 1$, the combined statistic effectively eliminates the cluster contribution, although at the expense of lowering filament significance from $\sim 5 - 7\sigma$ to $\sim 2 - 3\sigma$. Figure 6 shows $L(\alpha)$ for $\alpha \in [0, 1]$, illustrating these trends.

Therefore, despite its ability to distinguish cluster contamination from genuine filamentary signal, the negative cross gradient is unusable in our case due to the relatively low source density of the LoVoCCS shear catalog. However, for deep space-based observations (e.g., JWST) with substantially higher source densities, the corresponding loss in detection significance may be negligible, making the use of the negative cross gradient viable. Thus, in the subsequent analysis, we use the cross statistic solely as a qualitative indicator of potential cluster contamination.

6.5. *Estimating Filament Properties*

We use the Markov Chain Monte Carlo (MCMC) sampler *emcee* (D. Foreman-Mackey et al. 2013) to infer filament properties – κ_0 and h_c. For each detected filament, we fit the model described in Eq. (4) to the shear data within a fixed window of width $h_{\rm ref} = 1.5$ Mpc about the detection axis. This window size allows the sampler to explore all plausible filament widths ($h_c < 0.75$ Mpc), resolving both the constant κ_0 region up to h_c and the $\propto h^{-2}$ decline, while also limiting contamination from adjacent filament(s). The resulting posterior distributions for κ_0 and h_c are displayed in Figure 7, with the corresponding median values summarized in Table 1. To avoid clutter and improve interpretability, we present the posterior distribution for one branch per filament ($\theta = 190°$, $\theta = 250°$). For reference, we mark the input parameters ($\kappa_0 = 0.03$, $h_c = 0.25$ Mpc) with a '×' in the contour plot. We find all model parameters to be

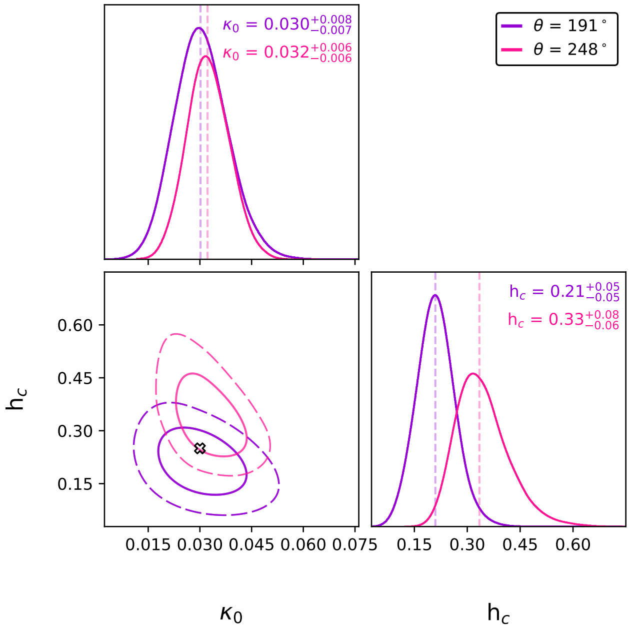

Figure 7. Mock Catalog: Posterior distributions of the filament parameters obtained via MCMC sampling. The inner (solid) and outer (dashed) contours in the joint distribution enclose the 68% (1σ) and 95% (2σ) credible regions, respectively. Dashed vertical lines indicate the median values of the marginalized distributions. The black-outlined cross in the contour plot marks the input filament parameters, $\kappa_0 = 0.03$ and $h_c = 0.25$ Mpc. The legend in the upper-right corner shows the color coding for the two detections.

well constrained. The maximum deviations of the estimated median values from the input parameters are $\Delta\tilde{\kappa}_0 = 0.004$ (13%) and $\Delta\tilde{h}_c = 0.08$ (32%). While most of this scatter can be attributed to shape noise, comparison with the noise-free case indicates that the estimated filament parameters are also slightly biased by other structures in the field.

7. DATA

We used observations from the Dark Energy Camera (DECam) (B. Flaugher et al. 2015) on the 4-m Blanco Telescope at the Cerro Tololo Inter-American Observatory (CTIO) as part of the Local Volume Complete Cluster Survey (LoVoCCS; Proposal ID: 2019A-0308; PI: Ian Dell'Antonio), an NSF NOIRLab survey of 107 nearby ($0.03 < z < 0.12$) X-ray luminous clusters ([$0.1 - 2.4$ keV] $L_{X500c} > 10^{44}$ erg s^{-1}) in *ugriz* bands (S. Fu et al. 2022). The LoVoCCS targets are imaged to depths comparable to the upcoming Vera C. Rubin Observatory's Legacy Survey of Space and Time (LSST) Year 1–2 data, reaching a 5σ coadded median depth of $\sim 25 - 26$ magnitude for point sources and about ~ 0.3 mag shallower for extended objects in each band (Table 1 & 2; S. Fu et al. 2024). We use the LSST Science Pipeline in conjunction with the LoVoCCS data analysis pipeline to process raw exposures and obtain a uniformly processed catalog of coordinates, magnitudes, shapes, photometric redshifts, and other associated quantities of all deblended and well-measured coadd objects within each cluster. We then apply the quality cuts described in S. Fu et al. (2022, Section 3.2; `mass_map`), with modifications, to extract a clean sample of source galaxies with calibrated reduced shears. We made the following changes to the selection criteria:

(1) Expand Background Population: S. Fu et al. (2022) applied a cut on z_b (most probable redshift); $0.15 < z_b < 1.4$ to avoid contamination from cluster members and exclude unreliable photo-z at high redshift. We use the updated criteria in S. Fu et al. (2024) and require that $0.1 + z_l < z_b < 1.4$ where z_l is the cluster redshift. The introduction of a z_l-based variable limit has been reported to increase lensing S/N by $\leq 10\%$.

(2) Lower BPZ `odds`: Within the framework of Bayesian Photometric Redshift estimation (BPZ; N. Benítez et al. 2004), `odds` represents the likelihood of the estimated redshift, z_b, being correct. We relax the minimum `odds` requirement from > 0.95 to > 0.8 to admit sources with moderately uncertain photo-z estimates. The resulting increase in true background sources outweighs the impact of misclassified foreground galaxies, thereby boosting the lensing S/N.

(3) Position Cut: Finally, since we are only concerned with filament detection in the intercluster region between clusters, we limit the catalog to sources within a radius of 1.25 times the intercluster distance between the primary cluster and the outermost secondary cluster under consideration. This cut does not affect the outcome, since the filter itself is spatially constrained, but it helps reduce computational overhead.

While the original source catalog contains galaxies with a number density of $n_g \sim 50$ arcmin^{-2}, our selection criteria yield a clean sample with $n_g \sim 7 - 12$ arcmin^{-2}.

N-body simulations show that clusters separated by $\leq 5\,h^{-1}$Mpc are invariably connected by at least one filament (J. M. Colberg et al. 2005). Furthermore, massive clusters are typically embedded within rich filamentary networks with high-density contrast, thereby producing a strong lensing signal. Motivated by these considerations, we select the most massive and X-ray luminous cluster pairs in the LoVoCCS survey as prime targets for filament detection. In this work, we focus on three such systems: (i) Abell 401–399, (ii) Abell 2029–2033-SIG, and (iii) Abell 3558–3556–3562 (Shapley Supercluster Core). Additionally, to build confidence in our analysis, we include a lower-mass system, Abell 2351, as a null test to demonstrate that our method does not produce spurious filament detections. Hereafter, we denote each system by the primary cluster around which the analysis is centered.

8. RESULTS

Following the procedure outlined in Section 6, we apply the matched-filter method to the dataset described above. We use the coordinates of the brightest cluster galaxy (BCG) to define the centers of all clusters in the field. Cluster redshifts are sourced from the MCXC catalog (R. Piffaretti et al. 2011). For each system, we determine the radial filter cutoffs, r_1 and r_2, by requiring that the shear contribution from clusters in the field stays below 2% within the annular search space. A full description is provided in Appendix A; the resulting cutoff values for each system are listed in Table 5.

8.1. *Abell 401*

Abell 401 (A401; $z = 0.0739$) and Abell 399 (A399; $z = 0.0722$) are separated approximately by 3.07 Mpc (or $\sim$ 37 arcmin) and are widely regarded to be in a pre-merger phase. X-ray and SZ observations provide strong evidence for a hot gas filament connecting the two clusters (H. Akamatsu et al. 2017; V. Bonjean et al. 2018; A. D. Hincks et al. 2022; F. Radiconi et al. 2022). Analysis of the galaxy populations shows no significant difference in star-formation activity between the clusters and the intercluster filament (V. Bonjean et al. 2018). S. Fu et al. (2024) confirms this by identifying a bridge of red-sequence galaxies connecting the two clusters. The weak-lensing mass map presented in S. Fu et al. (2024) reveals a stronger lensing signal for A401 than for A399; however, no clear lensing signal is seen from the intercluster filament. We report the *first* weak-lensing (WL) detection of the intercluster bridge connecting A401 and A399.

We present our results in the composite Figure 9. Panel (a) displays the statistics $\Gamma_+(\theta)$ and $\Gamma_\times(\theta)$, computed using the optimal matched filter with $r_1 = 1.27$ Mpc and $r_2 = 1.93$ Mpc. The tangential signal Γ_+ exhibits two prominent peaks at $\theta = 289°$ (south; S) and $\theta = 102°$ (north; N), with significances of 6.7σ and 4.2σ, respectively. A lower-significance (2σ) peak is detected towards the east; however, the absence of a corresponding sharp decline in the cross component $\Gamma_\times$ suggests that this feature may instead be associated with a halo. Panel (c) displays the spatial distribution of spectroscopic members drawn from the NASA/IPAC Extragalactic Database (G. Helou et al. 1991; NASA/IPAC Extragalactic Database (NED) 2019) and DESI DR1 (

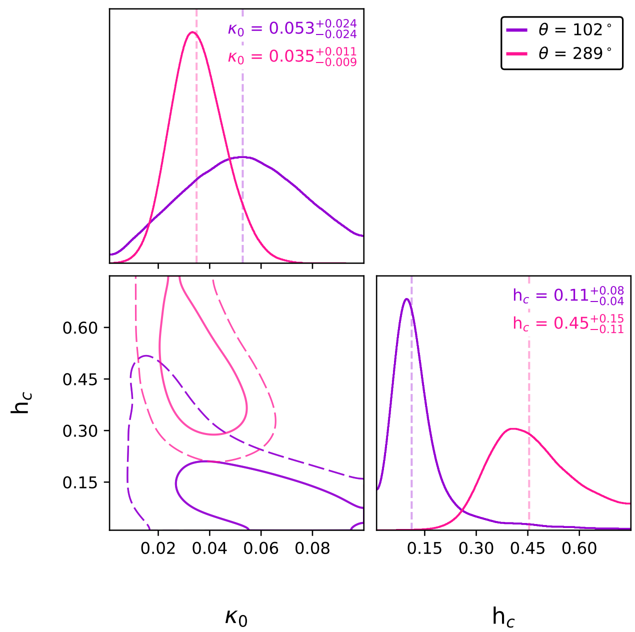

Figure 8. A401: Posterior distributions of the filament parameters obtained via MCMC sampling. The inner (solid) and outer (dashed) contours in the joint distribution enclose the 68% (1σ) and 95% (2σ) credible regions, respectively. Dashed vertical lines indicate the median values of the marginalized distributions. The legend in the upper-right corner shows the color coding for the two detections.

DESI Collaboration et al. 2025) in the A401-399 system (redshift criteria: $0.06 < z < 0.085$). Both filaments are aligned with overdensities in the spec-z member distribution as well as the red-sequence galaxy distribution reported by S. Fu et al. (2024). Figure 8 presents the posterior distributions for the maximum convergence κ_0 and characteristic width h_c for both filaments (results summarized in Table 2). The S filament is well constrained, with $\kappa_0 = 0.035^{+0.011}_{-0.009}$ and $h_\mathrm{c} = 0.45^{+0.15}_{-0.11}$, whereas the N filament is less tightly constrained, with $\kappa_0 = 0.053^{+0.024}_{-0.024}$ and $h_\mathrm{c} = 0.11^{+0.08}_{-0.04}$.

Table 2. Filament Properties - A401

Direction	Orientation	Significance	κ_0	h_c
	(deg)	(σ)		(Mpc)
N	102	4.2	$0.053^{+0.024}_{-0.024}$	$0.11^{+0.08}_{-0.04}$
S	289	6.7	$0.035^{+0.011}_{-0.009}$	$0.45^{+0.15}_{-0.11}$

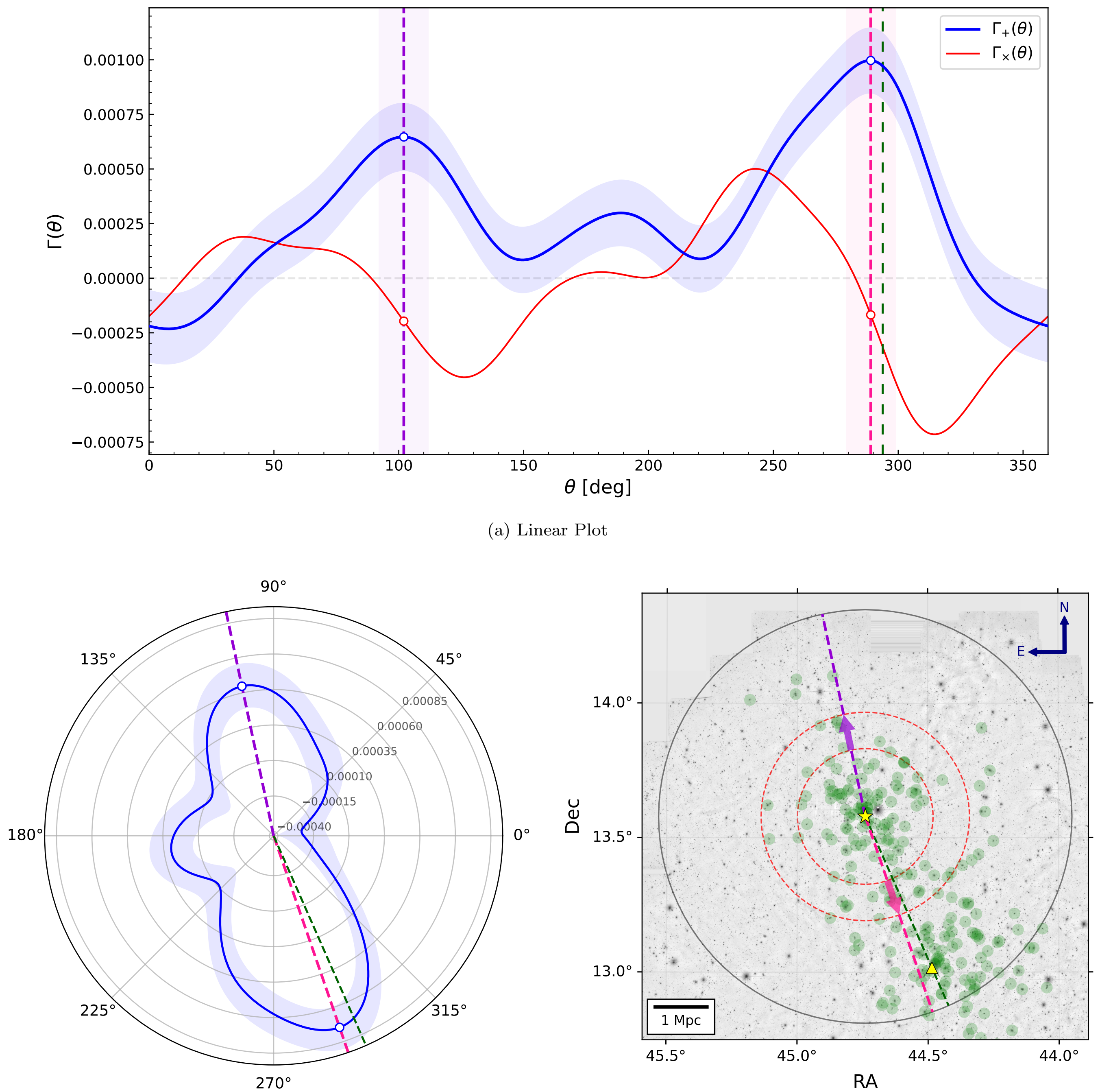

(a) Linear Plot

(b) Polar Plot

(c) Overlaid Plot

Figure 9. Filament detection results for the A401 system. *Top:* Matched-filter statistics $\Gamma_+(\theta)$ and $\Gamma_\times(\theta)$ as a function of the search angle θ. The blue and red solid lines correspond to the tangential and cross components, respectively, with the light blue shade indicating the 1σ uncertainty in the tangential signal. The violet and pink vertical dashed lines mark the tangential signal peaks detected at $\theta = 102^\circ$ and $\theta = 289^\circ$, respectively. The corresponding light shade indicates a $\pm 10^\circ$ window centered on the detected peak, provided for comparison with orientations of other clusters in the field. The green dashed line marks the orientation of A399 relative to A401. *Bottom-left:* Polar representation of the top panel. *Bottom-right:* Detected filament orientations overlaid on the inverted r-band coadded image used for shape measurement. The dashed red circles represent the radial cutoffs $r_1 = 1.27$ Mpc and $r_2 = 1.93$ Mpc. The violet and pink arrows extending from r_1 to r_2 indicate the spatial orientation of the detected filaments. A401 (primary) and A399 (secondary) are marked with a yellow star and triangle, respectively. Spectroscopic member galaxies ($0.06 < z < 0.085$) in the field are marked with green circles. The gray circle represents the position cut applied to the source catalog used for filament detection.

8.2. *Abell 2029*

Abell 2029 (A2029; $z = 0.0766$) is one of the most massive galaxy clusters in the local universe. Together with its close neighbor, Abell 2023 (A2033; $z = 0.0817$), located approximately 3.16 Mpc (or $\sim$ 37 arcmin) to the north, the system has been extensively studied in the X-rays. Deep *Chandra* imaging reveals a sloshing spiral pattern centered on A2029, indicative of complex dynamical evolution (R. Paterno-Mahler et al. 2013). Early studies with ROSAT and *Suzaku* observations (S. A. Walker et al. 2012) reported excess emission along the axis connecting A2029 and A2023. More recently, M. S. Mirakhor et al. (2022) confirmed this feature at a significance of $6.5 - 7\sigma$, providing strong evidence for an intercluster gas filament. The complex structure of the system has also been widely analyzed in the optical regime through lensing measurements (J. McCleary et al. 2020; J. Sohn et al. 2019; S. Fu et al. 2024). Using intensive spectroscopy in combination with WL and X-ray measurements, J. Sohn et al. (2019) demonstrated that A2033 and the Southern Infalling Group (SIG) are dynamical substructures bound to be accreted onto A2029. Building on previous lensing studies, S. Fu et al. (2024) reported a high lensing signal for A2029 (7.6σ), a moderate signal for A2033 ($\sim 3\sigma$), and a tight alignment of 3-4σ contours with the intercluster direction. The SIG is detected at a lower significance of $\sim 1.8\sigma$.

Figure 11 summarizes our results. We detect two prominent filaments connecting A2029 to the SIG ($\theta = 261°$; south) and A2033 ($\theta = 108°$; north), with detection significances of 7.3σ and 6.4σ, respectively. Notably, the southern (S) filament is detected at a higher significance despite the SIG having a lower WL mass than A2033 (J. Sohn et al. 2019). This trend is also reflected in our parameter estimation analysis (see Figure 10 and Table 3), which yields a much higher characteristic width for the S filament ($h_c = 0.44^{+0.08}_{-0.07}$) than the N filament ($h_c = 0.25^{+0.07}_{-0.06}$). The maximum convergences are, however, similar: $\kappa_0 = 0.036^{+0.007}_{-0.006}$ (S) and $\kappa_0 = 0.039^{+0.010}_{-0.009}$ (N). Both filamentary structures are spatially consistent with the distribution of the spectroscopic members ($0.07 < z < 0.09$) presented in Figure 11(c) and with the red-sequence galaxy distribution presented in S. Fu et al. (2024). A less prominent peak (1.8σ) is observed in the north-west direction, coincident with an overdensity in the spec-z member distribution. The absence of a pronounced decline in the cross statistic, however, indicates that this signal is not associated with a filamentary structure.

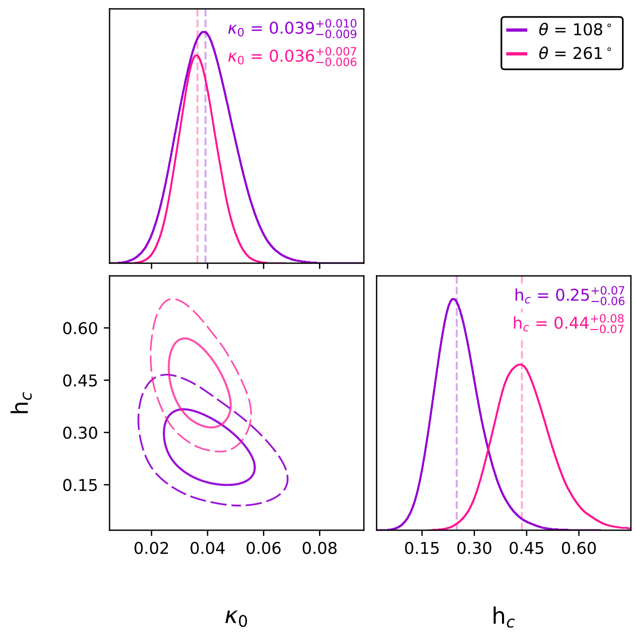

Figure 10. A2029: Posterior distributions of the filament parameters obtained via MCMC sampling. The inner (solid) and outer (dashed) contours in the joint distribution enclose the 68% (1σ) and 95% (2σ) credible regions, respectively. Dashed vertical lines indicate the median values of the marginalized distributions. The legend in the upper-right corner shows the color coding for the two detections.

Table 3. Filament Properties - A2029

Direction	Orientation (deg)	Significance (σ)	κ_0	h_c (Mpc)
N	108	6.4	$0.039^{+0.010}_{-0.009}$	$0.25^{+0.07}_{-0.06}$
S	261	7.3	$0.036^{+0.007}_{-0.006}$	$0.44^{+0.08}_{-0.07}$

8.3. *Abell 3558*

Abell 3558 (A3558; $z = 0.048$) lies at the heart of the Shapley Supercluster (SSC) – the largest conglomeration of Abell clusters in the local universe. Together with Abell 3562 (A3562; $z = 0.049$) to the east, Abell 3556 (A3556; $z = 0.048$) to the west, and two poor clusters embedded in between (SC 1327-312 and SC 1329-313), they form the Shapley Supercluster Core – a continuous linear structure spanning $\sim$ 8 Mpc (or $\sim$ 2 deg) permeated by hot gas. In contrast to the gas bridges reported in previous systems, direct detection of filaments in the SSC Core is sparse and contested (A. Kull

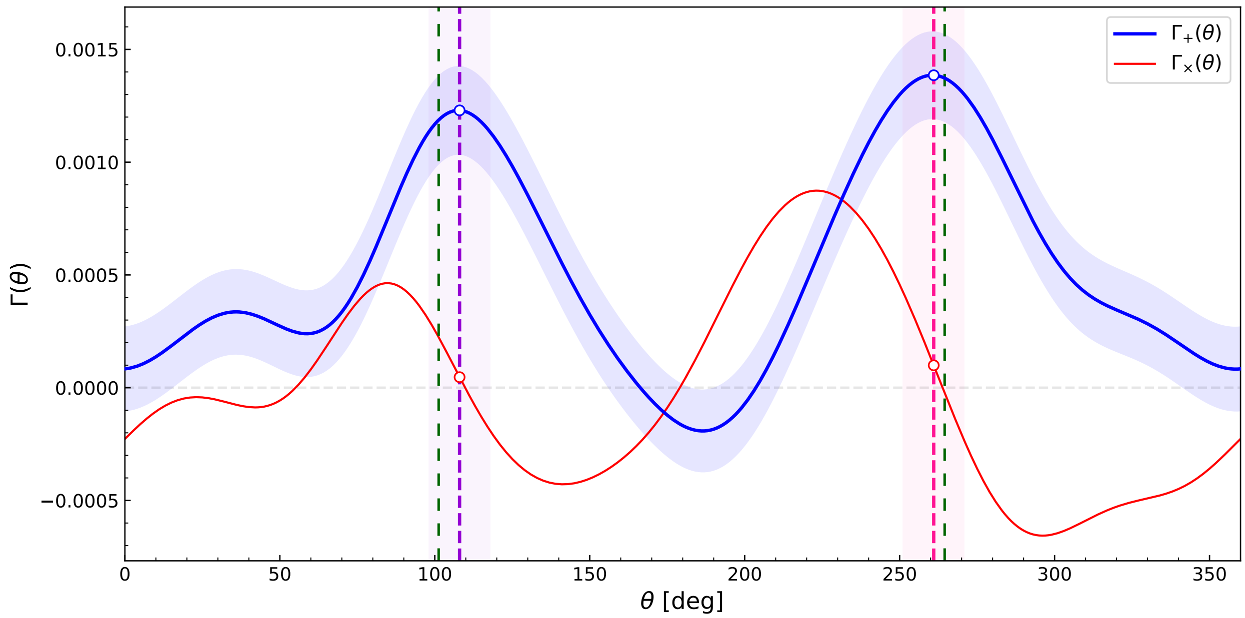

(a) Linear plot

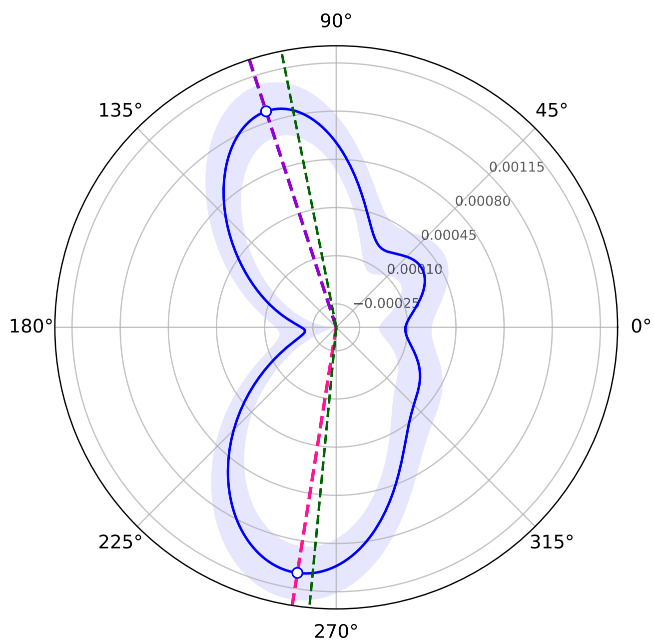

(b) Polar plot

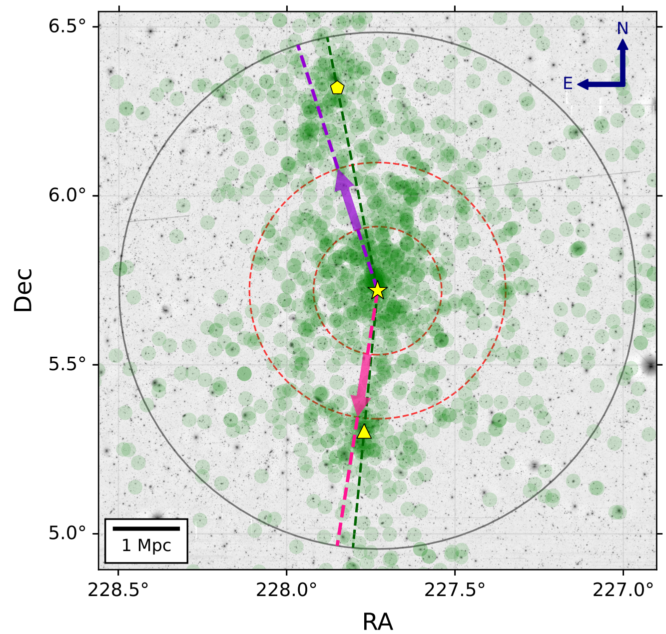

(c) Overlaid plot

Figure 11. Filament detection results for the A2029 system. *Top:* Matched-filter statistics $\Gamma_+(\theta)$ and $\Gamma_\times(\theta)$ as a function of the search angle θ. The blue and red solid lines correspond to the tangential and cross components, respectively, with the light blue shade indicating the 1σ uncertainty in the tangential signal. The violet and pink vertical dashed lines mark the tangential signal peaks detected at $\theta = 108^\circ$ and $\theta = 261^\circ$, respectively. The corresponding light shade indicates a $\pm10^\circ$ window centered on the detected peak, provided for comparison with orientations of other clusters in the field. The green dashed lines mark the orientations of A2033 and SIG relative to A2029, ordered counterclockwise from 0° to 360°. *Bottom-left:* Polar representation of the top panel. *Bottom-right:* Detected filament orientations overlaid on the inverted r-band coadded image used for shape measurement. The dashed red circles represent the radial cutoffs $r_1 = 0.99$ Mpc and $r_2 = 1.98$ Mpc. The violet and pink arrows extending from r_1 to r_2 indicate the spatial orientation of the detected filaments. A2029 (primary), A2033 (secondary) and SIG (secondary) are marked with a yellow star, pentagon, and triangle, respectively. Spectroscopic member galaxies ($0.07 < z < 0.09$) in the field are marked with green circles. The gray circle represents the position cut applied to the source catalog used for filament detection.

& H. Böhringer 1999; E. Ursino et al. 2015; I. Mitsuishi et al. 2012). In particular, the bridge between A3558 and A3556 remains ambiguous: reported X-ray excesses have been attributed to cluster outskirts or unresolved point sources.

Optical studies, in comparison, have been more successful at finding these elusive features. Spectroscopic studies reveal that all 11 clusters in the SSC are inter-connected and lie embedded within a cosmic sheet at $z \sim 0.048$, in the process of collapsing into A3558. C. P. Haines et al. (2018) find a filament-like overdensity extending from A3562 through A3558 to A3556, with a sharp low-density edge between A3558 and A3556. They also report evidence for a second stream of galaxies extending northward from A3558 towards A3559, with two small groups, Filament Group 1 & 2 (FG1 & FG2), embedded between them. WL maps reveal the continuous structure of the SSC Core, with a prominent peak at the BCG of A3558 and secondary peaks centered at A3556 and A3562 (P. Merluzzi et al. 2015; Y. Higuchi et al. 2020; S. Fu et al. 2024). Consistent with spectroscopic studies, Y. Higuchi et al. (2020) detected WL contours at the 1σ level, providing complementary evidence for filamentary structures linking A3558 with neighboring clusters (A3556, A3559 and A3562).

Figure 13 summarizes our results. We detect two peaks in the tangential signal at $\theta = -12^\circ$ (west; W) and $\theta = 111^\circ$ (north; N) with significances of 5.8σ and 4.0σ, respectively. The W detection is exactly aligned with A3556, while the N detection roughly follows the FG1-FG2 axis (eventually leading to A3559). A marginal tangential signal (1.6σ), accompanied by a substantial negative cross-gradient, is measured to the south. This is consistent with a $1-2\sigma$ contour between A3558 and A3560 in the WL map reported by Y. Higuchi et al. (2020). However, no filamentary structure is detected in the direction of A3562, despite the presence of a linear overdensity in the spec-z member distribution ($0.04 < z < 0.06$), as shown in Figure 13(c). We attribute the absence of a straight filament between A3558 and A3562 to the complex morphology of the region, which includes the smaller clusters SC 1327–312 and SC 1329–313. The W filament has a higher maximum convergence ($\kappa_0 = 0.023^{+0.005}_{-0.005}$) than the N filament ($\kappa_0 = 0.015^{+0.005}_{-0.005}$). Both filaments exhibit similar inferred widths, with $h_c = 0.24^{+0.07}_{-0.06}$ for the W filament, and $h_c = 0.23^{+0.13}_{-0.06}$ for the N filament.

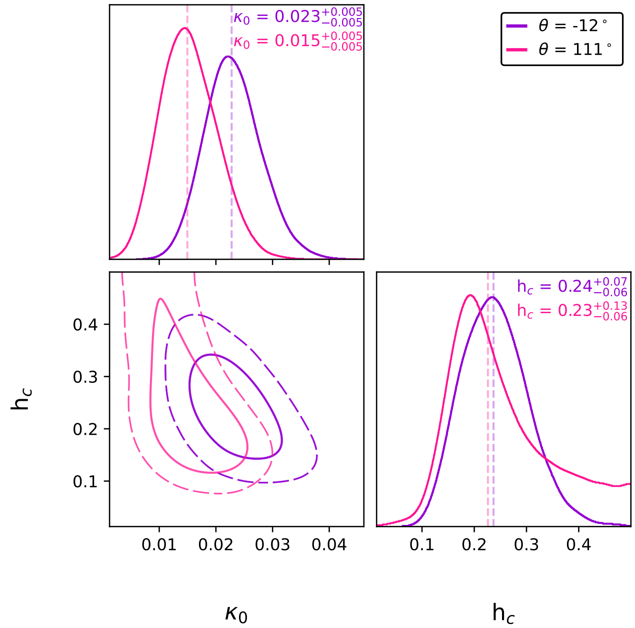

Figure 12. A3558: Posterior distributions of the filament parameters obtained via MCMC sampling. The inner (solid) and outer (dashed) contours in the joint distribution enclose the 68% (1σ) and 95% (2σ) credible regions, respectively. Dashed vertical lines indicate the median values of the marginalized distributions. The legend in the upper-right corner shows the color coding for the two detections.

Table 4. Filament Properties – A3558

Direction	Orientation (deg)	Significance (σ)	κ_0	h_c (Mpc)
W	-12	5.8	$0.023^{+0.005}_{-0.005}$	$0.24^{+0.07}_{-0.06}$
N	111	4.0	$0.015^{+0.005}_{-0.005}$	$0.23^{+0.13}_{-0.06}$

8.4. *Abell 2351*

Compared to the systems studied above, Abell 2351 (A2351; $z = 0.0897$) is relatively less massive, with an X-ray mass of $M_{\mathrm{X500c}} = 2.75 \times 10^{14}\,\mathrm{M}_\odot$ (R. Piffaretti et al. 2011) and a WL mass of $M_{\mathrm{WL200c}} = 2.8 \times 10^{14}\,\mathrm{M}_\odot$ (LoVoCCS Collaboration; private communication; Oct 1, 2025). We select A2351 as a control system because of its low mass and limited substructure in the WL mass map (S. Fu et al. 2024). Figure 14 presents our results. We find no significant detections ($> 2\sigma$) in the tangential statistic $\Gamma_+(\theta)$. The absence of spurious peaks in A2351 suggests that the reported detections in previous systems are unlikely to be artifacts introduced by our methods.

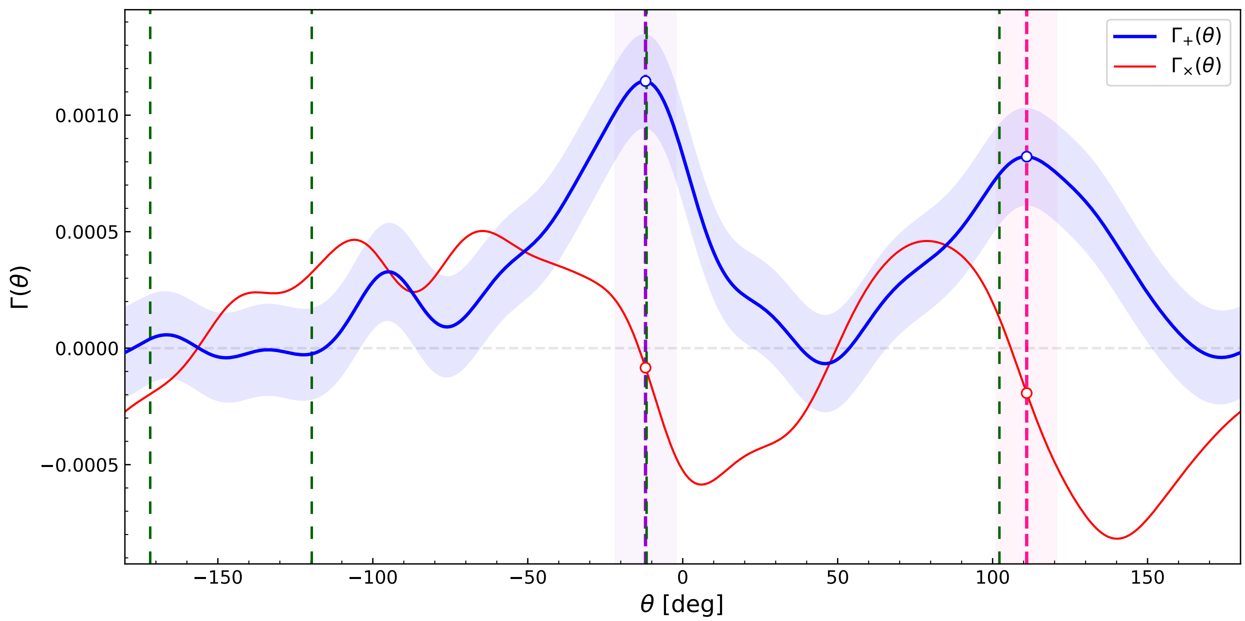

(a) Linear plot

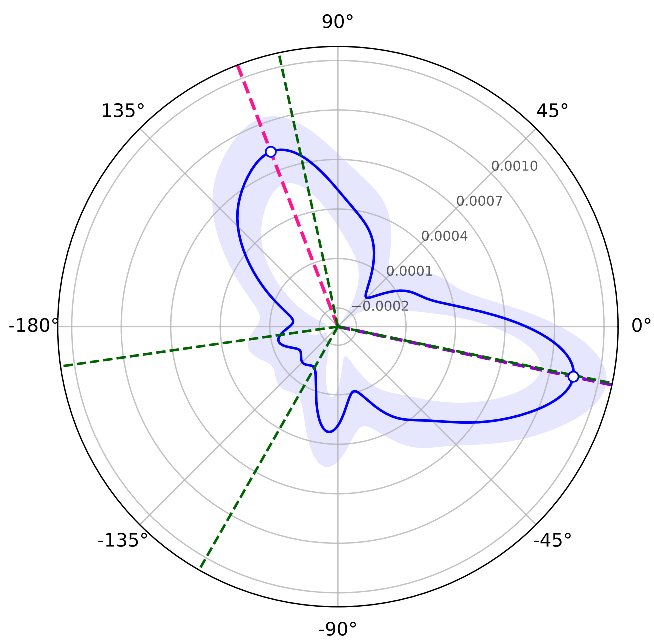

(b) Polar plot

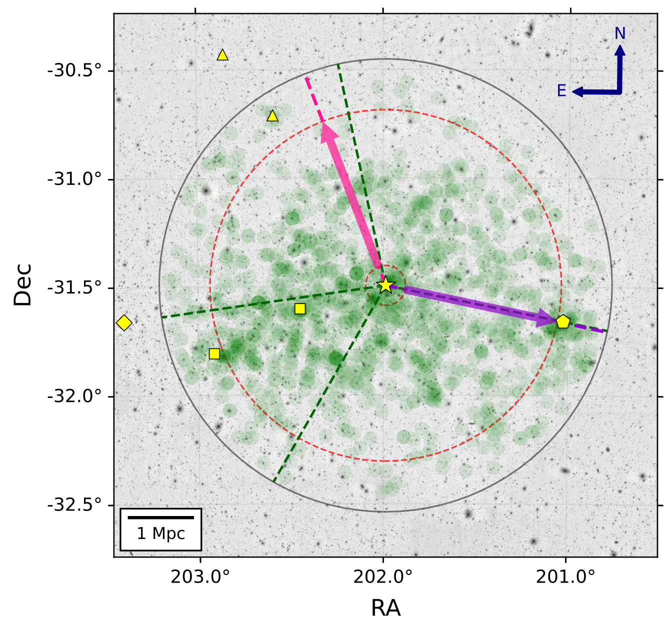

(c) Overlaid plot

Figure 13. Filament detection results for the A3558 system. *Top:* Matched-filter statistics $\Gamma_+(\theta)$ and $\Gamma_\times(\theta)$ as a function of the search angle θ. The blue and red solid lines correspond to the tangential and cross components, respectively, with the light blue shade indicating the 1σ uncertainty in the tangential signal. The violet and pink vertical dashed lines mark the tangential signal peaks detected at $\theta = -12^\circ$ and $\theta = 111^\circ$, respectively. The corresponding light shade indicates a $\pm 10^\circ$ window centered on the detected peak, provided for comparison with orientations of other clusters in the field. The green dashed lines mark the orientations of A3562, A3560, A3556 and A3559 relative to A3558, ordered counterclockwise from -180° to 180°. *Bottom-left:* Polar representation of the top panel. *Bottom-right:* Detected filament orientations overlaid on the inverted r-band coadded image used for shape measurement. The dashed red circles represent the radial cutoffs $r_1 = 0.3$ Mpc and $r_2 = 2.75$ Mpc. The violet and pink arrows extending from r_1 to r_2 indicate the spatial orientation of the detected filaments. A3558 (primary), A3556 (secondary), A3562 (secondary), SC 1327-312/SC 1329-313 (secondary) and FG1/FG2 (secondary) are marked with a yellow star, pentagon, diamond, squares, and triangles, respectively. Spectroscopic member galaxies ($0.04 < z < 0.06$) in the field are marked with green circles. The gray circle represents the position cut applied to the source catalog used for filament detection.

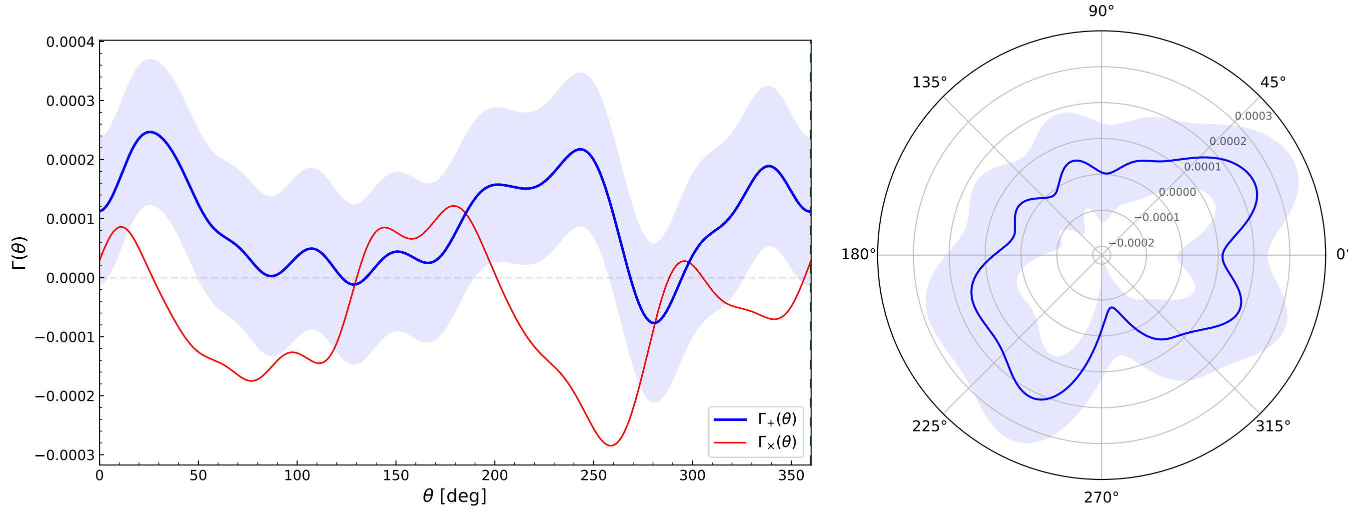

Figure 14. Filament detection results for A2351. *Left:* Matched-filter statistics $\Gamma_\times(\theta)$ and $\Gamma_+(\theta)$ as a function of the search angle θ. The blue and red solid lines correspond to the tangential and cross components, respectively, with the light blue shade indicating the 1σ uncertainty in the tangential signal. *Right:* Polar representation of the left panel.

9. CONCLUSIONS

In this study, we applied a matched-filter method to detect the weak-lensing signal of intercluster filaments in three massive systems centered on Abell 401, Abell 2029, and Abell 3558. To improve its performance in the presence of noise, the matched filter was optimized using mock simulations of the observed shear field. We also investigated the use of the B-mode signal of filaments to enhance detection significance and distinguish genuine filamentary signal from cluster contamination.

Our main results are as follows:

(1) In each system, we detect two prominent filaments with significances in the range $4\sigma - 7.3\sigma$. In particular, we report the *first* definitive WL detections ($> 5\sigma$) of the intercluster bridges in the following cluster pairs: A401/399, A2029/2033, A2029/SIG, and A3558/3556.

(2) Except for A3558/3562, we identify intercluster filaments connecting each primary-secondary cluster pair within 10° of the intercluster direction measured from the primary cluster.

(3) The orientation of detected intercluster filaments is consistent with the spatial distribution of spectroscopic cluster members drawn from NED (G. Helou et al. 1991) and DESI DR1 (DESI Collaboration et al. 2025), as well as the red-sequence galaxy distribution reported by S. Fu et al. (2024).

(4) We measured the physical properties of detected filaments via MCMC sampling, obtaining maximum convergences in the range $\kappa_0 \sim 0.015 - 0.053$ and characteristic widths spanning $h_c \sim 0.11 - 0.45$ Mpc. Among all systems studied in this paper, A2029 exhibits the strongest filament detections with the most tightly constrained physical parameters.

These findings are consistent with the *cosmic web* picture of structure formation and provide direct observational evidence to support predictions from N-body simulations (J. M. Colberg et al. 2005) that massive clusters are typically embedded in a rich network of filaments with high-density contrast.

We note several limitations of the present work. While our sample of three cluster systems is sufficient to demonstrate the efficacy of the matched-filter method for filament detection, a substantially larger sample is required to characterize the ensemble properties of filaments. In a follow-up paper, we plan to extend our analysis to additional clusters from the LoVoCCS survey to develop a more comprehensive understanding of low-redshift ($z \lesssim 0.1$) filamentary structures. Given the relatively low source density in our survey after applying selection cuts, careful characterization of the shape noise is imperative for effective filter optimization. In this study, we approximate the noise as Gaussian; however, future efforts will aim to model the spectral properties of shear noise in our observations in greater detail. To mitigate the effect of shear contamination from nearby clusters, we apply radial cuts to the matched filter. In future work, we plan to incorporate adjacent clusters directly into the mass model and account for the redshift distribution of background sources to enable an accurate estimation of the linear mass density of filaments.

ACKNOWLEDGMENTS

We are grateful to Shenming Fu for his constructive feedback on this paper. We would like to thank the members of the Observational Cosmology, Gravitational Lensing, and Astrophysics Group at Brown University, in particular Anthony Englert, Zacharias Escalante and Shenming Fu, for their contribution in processing the data for all galaxy clusters analyzed in this work using the LoVoCCS pipeline.

We acknowledge support from the National Science Foundation (No. AST-2108287; Collaborative Research; LoVoCCS).

This project used data obtained with the Dark Energy Camera (DECam), which was constructed by the Dark Energy Survey (DES) collaboration. Funding for the DES Projects has been provided by the DOE and NSF (USA), MISE (Spain), STFC (UK), HEFCE (UK), NCSA (UIUC), KICP (U. Chicago), CCAPP (Ohio State), MIFPA (Texas A&M), CNPQ, FAPERJ, FINEP (Brazil), MINECO (Spain), DFG (Germany) and the Collaborating Institutions in the Dark Energy Survey, which are Argonne Lab, UC Santa Cruz, University of Cambridge, CIEMAT-Madrid, University of Chicago, University College London, DES-Brazil Consortium, University of Edinburgh, ETH Zürich, Fermilab, University of Illinois, ICE (IEEC-CSIC), IFAE Barcelona, Lawrence Berkeley Lab, LMU München and the associated Excellence Cluster Universe, University of Michigan, NSF NOIRLab, University of Nottingham, Ohio State University, OzDES Membership Consortium, University of Pennsylvania, University of Portsmouth, SLAC National Lab, Stanford University, University of Sussex, and Texas A&M University.

Based on observations at NSF Cerro Tololo Inter-American Observatory, NSF NOIRLab (NOIRLab Prop. ID 2019A-0308; PI: I. Dell'Antonio), which is managed by the Association of Universities for Research in Astronomy (AURA) under a cooperative agreement with the U.S. National Science Foundation.

This research used data obtained with the Dark Energy Spectroscopic Instrument (DESI). DESI construction and operations is managed by the Lawrence Berkeley National Laboratory. This material is based upon work supported by the U.S. Department of Energy, Office of Science, Office of High-Energy Physics, under Contract No. DE–AC02–05CH11231, and by the National Energy Research Scientific Computing Center, a DOE Office of Science User Facility under the same contract. Additional support for DESI was provided by the U.S. National Science Foundation (NSF), Division of Astronomical Sciences under Contract No. AST-0950945 to the NSF's National Optical-Infrared Astronomy Research Laboratory; the Science and Technology Facilities Council of the United Kingdom; the Gordon and Betty Moore Foundation; the Heising-Simons Foundation; the French Alternative Energies and Atomic Energy Commission (CEA); the National Council of Humanities, Science and Technology of Mexico (CONAHCYT); the Ministry of Science and Innovation of Spain (MICINN), and by the DESI Member Institutions: www.desi.lbl.gov/collaborating-institutions. The DESI collaboration is honored to be permitted to conduct scientific research on I'oligam Du'ag (Kitt Peak), a mountain with particular significance to the Tohono O'odham Nation. Any opinions, findings, and conclusions or recommendations expressed in this material are those of the author(s) and do not necessarily reflect the views of the U.S. National Science Foundation, the U.S. Department of Energy, or any of the listed funding agencies.

This research has made use of the NASA/IPAC Extragalactic Database (NED), which is operated by the Jet Propulsion Laboratory, California Institute of Technology, under contract with the National Aeronautics and Space Administration.

This research uses services or data provided by the Astro Data Lab, which is part of the Community Science and Data Center (CSDC) Program of NSF NOIRLab. NOIRLab is operated by the Association of Universities for Research in Astronomy (AURA), Inc. under a cooperative agreement with the U.S. National Science Foundation.

This research was conducted using computational resources and services at the Center for Computation and Visualization, Brown University.

Facilities: Blanco, Astro Data Archive, Astro Data Lab

Software: `astropy` (Astropy Collaboration et al. 2013, 2018, 2022), `galsim` (B. T. P. Rowe et al. 2015), `numpy` (C. R. Harris et al. 2020), `scipy` (P. Virtanen et al. 2020), `emcee` (D. Foreman-Mackey et al. 2013), `pandas` (The pandas development Team 2025; Wes McKinney 2010), `matplotlib` (J. D. Hunter 2007), `corner` (D. Foreman-Mackey 2016).

The filament detection code, mock simulation code and all accompanying scripts used to produce the figures presented in this paper are publicly available[5].

APPENDIX

A. OPTIMAL CUTOFF FREQUENCY

As noted in Section 5.2.1, the definition $k_{\rm cut} = \sqrt{n_{\rm g}\ln 2}$ yields a suboptimal filter for our dataset. Here we describe how mock data can be used to determine the optimal cutoff frequency. Following the procedure outlined in Section 6.1, we generate multiple realizations of mock shear data for a configuration with a filament centered on a primary cluster ($M_{\rm 200c} = 5 \times 10^{14}$ $\rm M_\odot$) and oriented at an angle $\theta_{\rm f} = 135°$. The filament convergence and characteristic width are fixed to $\kappa_0 = 0.03$ and $h_{\rm c} = 0.25$ Mpc. We add zero-mean Gaussian noise with $\sigma_\gamma = 0.45$ to simulate the LoVoCCS dataset. The unoptimized matched filter with width $h_{\rm c,filter} = 0.15$ Mpc is restricted to the annulus $r_1 < r < r_2$, with $r_1 = 0.91$ Mpc and $r_2 = 3.64$ Mpc.

For each mock realization, we run the filament-detection analysis described in Section 6 with a range of cutoff frequencies (0.08 arcmin^{-1} $< k_{\rm cut} <$ 3.72 arcmin^{-1}) used to optimize the filter. We record the peak S/N of the detections corresponding to filament branches at $\theta = 135°$ and $\theta = 315°$ for each run. This process is repeated for 10 mock realizations (20 filament branches in total) to compute the mean S/N as a function of the cutoff frequency.

As shown in Figure 15(a), we obtain a unimodal profile for S/N($k_{\rm cut}$) with a maximum at $k_{\rm cut} = 0.21$ arcmin^{-1} and a steep decline in both directions. For the average source density in our dataset, $\langle n_{\rm g}\rangle \sim 10$ arcmin^{-2}, the earlier definition, $k_{\rm cut} = \sqrt{n_{\rm g}\ln 2}$ corresponds to a cutoff frequency of $k_{\rm cut} = 2.63$ arcmin^{-1}. Lowering the cutoff frequency from $k_{\rm cut} = 2.63$ arcmin^{-1} to $k_{\rm cut} = 0.21$ arcmin^{-1} reduces the angular resolution of the filter in real space, thereby effectively suppressing noise at low k-modes and improving the performance by ΔS/N ~ 1.

Another performance metric is the filter's ability to recover the input filament orientation. Figure 15(b) displays the orientation offset, $\Delta\theta(k_{\rm cut}) = |\theta_{\rm det} - \theta_{\rm f}|$, plotted as a function of the cutoff frequency $k_{\rm cut}$. Here, $\theta_{\rm det}$ and $\theta_{\rm f}$ denote the detected and true filament orientations, respectively. The filter constructed with $k_{\rm cut} = 0.21$ arcmin^{-1} (optimal cutoff frequency identified above) consistently yields small offsets across the examined frequency range, demonstrating its reliability. Thus, throughout this paper, we adopt a cutoff frequency of $k_{\rm cut} = 0.21$ arcmin^{-1} to optimize the matched filter.

B. RADIAL CUTOFFS

Shear contamination from the primary and secondary clusters can bias the inferred filament signal. We mitigate this effect by imposing radial cutoffs r_1 and r_2 on the matched filter to exclude shear-dominated regions near the clusters. To this end, we model all clusters as NFW halos and require that the tangential shear remains below the threshold $\gamma_+ < 0.02$ within the search space. The shear amplitude profile $\gamma_{\rm NFW}(r)$, for each cluster is evaluated using WL mass estimates from previous studies. When a WL mass estimate is only available for the primary cluster ($M_{\rm WL,p}$), we approximate the WL mass of the i-th secondary cluster ($M_{\rm WL,i}$) by scaling with the ratio of the X-ray masses:

$$M'_{{\rm WL},i} \approx M_{\rm WL,p}\frac{M_{{\rm X},i}}{M_{\rm X,p}}.$$

This preserves the relative mass ordering implied by X-ray data while anchoring the absolute scale to the WL measurement where available. With mass estimates determined for all clusters, we evaluate the minimum threshold radii $r_{\rm t}$, such that, $\gamma_+(r > r_{\rm t}) < 0.02$. The primary cluster determines the inner cutoff r_1, while the secondary clusters determine the outer cutoff r_2. Let R_i be the distance to the i-th secondary cluster from the primary cluster. The cutoffs are thus defined as

$$r_1 = r_{\rm t,p}\ ,$$
$$r_2 = \min_i\{R_i - r_{{\rm t},i}\},$$

where $r_{\rm t,p}$ and $r_{{\rm t},i}$ are the threshold radii for the primary and i-th secondary cluster, respectively. Table 5 summarizes the evaluated cutoff radii r_1 and r_2, along with all associated quantities, for all systems studied in the paper. In each system, we consider only massive clusters with WL masses $M_{\rm WL200c} > 10^{14}\,\rm M_\odot$ that could contribute to shear contamination.

[5] https://github.com/rahulshinde98/filament-detection.git

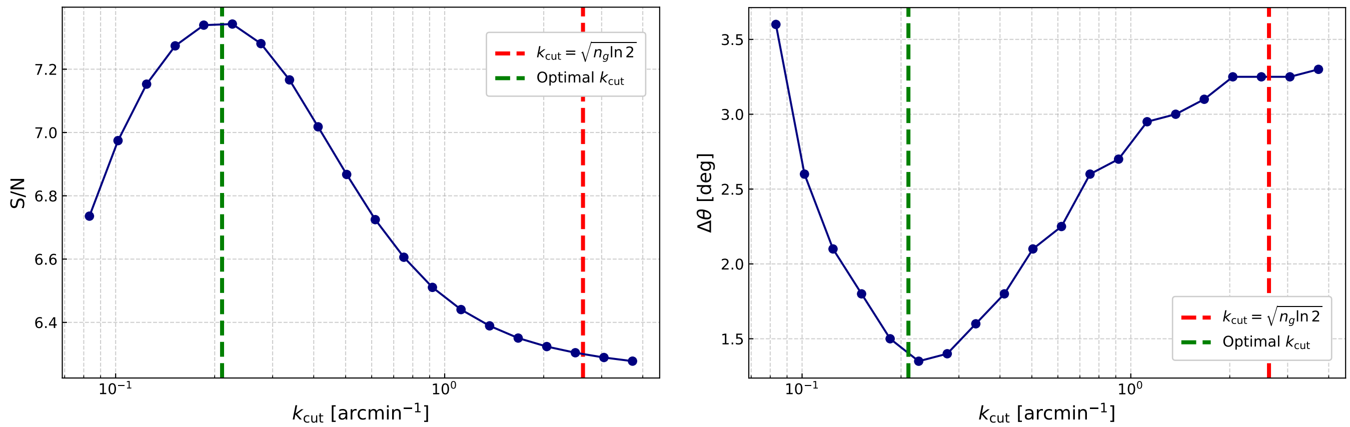

(a) Filter S/N Performance

(b) Orientation Error

Figure 15. Performance of the optimal matched filter as a function of the cutoff frequency, $k_{\rm cut}$, evaluated using multiple realizations of mock shear data. *Left:* Mean signal-to-noise ratio (S/N) of filament detections plotted against the cutoff frequency. The S/N profile exhibits a maximum at $k_{\rm cut} = 0.21$ arcmin^{-1} (green dashed line), indicating the optimal cutoff frequency used in our analysis. The red dashed line indicates the cutoff frequency obtained from the definition $k_{\rm cut} = \sqrt{n_{\rm g} \ln 2}$. *Right:* Absolute orientation offset between the detected and true filament orientations, $\Delta\theta(k_{\rm cut}) = |\theta_{\rm det} - \theta_{\rm f}|$, as a function of the cutoff frequency. The filter tuned to the optimal cutoff frequency identified in the left panel ($k_{\rm cut} = 0.21$ arcmin^{-1}) also minimizes the orientation error.

Table 5. Radial cutoffs evaluated from mass estimates to exclude cluster-induced shear contamination.

System	Role	Cluster	$M_{\rm WL200c}$ (10^{14} M$_\odot$)	$M_{\rm X200m}$ (10^{14} M$_\odot$)	$M'_{\rm WL200c}$ (10^{14} M$_\odot$)	r_t (Mpc)	R_i (Mpc)	r_1 (Mpc)	r_2 (Mpc)
1. Abell 401	p	Abell 401	14.3^a	21.3^b	—	1.27	—	1.27	1.93
	s	Abell 399	—	18.1^b	12.2	1.14	3.07		
2. Abell 2029	p	Abell 2029	9.6^c	—	—	0.99	—	0.99	1.98
	s	Abell 2033	2.4^c	—	—	0.33	3.16		
	s	SIG	1.3^c	—	—	0.18	2.16		
3. Abell 3558 (SSC)	p	Abell 3558	4.47^d	—	—	0.30	—	0.30	2.75
	s	Abell 3556	1.62^d	—	—	0.06	2.81		
	s	Abell 3562	2.04^d	—	—	0.11	4.09		
	s	Abell 3560	2.75^d	—	—	0.17	6.37		
4. Abell 2351 (Control)	p	Abell 2351	2.8^a	—	—	0.48	—	0.48	3.57*

$M'_{\rm WL200c}$ = interpreted weak lensing mass, p = primary cluster, s = secondary cluster, a = (LoVoCCS Collaboration, private communication, Oct 1, 2025), b = (A. D. Hincks et al. 2022), c = (J. Sohn et al. 2019), d = (Y. Higuchi et al. 2020), '—' = Not Applicable, * = arbitrarily chosen due to the absence of a secondary cluster constraint.

REFERENCES

Akamatsu, H., Fujita, Y., Akahori, T., et al. 2017, A&A, 606, A1, doi: 10.1051/0004-6361/201730497

Astropy Collaboration, Robitaille, T. P., Tollerud, E. J., et al. 2013, A&A, 558, A33, doi: 10.1051/0004-6361/201322068

Astropy Collaboration, Price-Whelan, A. M., Sipőcz, B. M., et al. 2018, AJ, 156, 123, doi: 10.3847/1538-3881/aabc4f

Astropy Collaboration, Price-Whelan, A. M., Lim, P. L., et al. 2022, ApJ, 935, 167, doi: 10.3847/1538-4357/ac7c74

Bartelmann, M., & Schneider, P. 2001, PhR, 340, 291, doi: 10.1016/S0370-1573(00)00082-X

Benítez, N., Ford, H., Bouwens, R., et al. 2004, ApJS, 150, 1, doi: 10.1086/380120

Bond, J. R., Kofman, L., & Pogosyan, D. 1996, Nature, 380, 603, doi: 10.1038/380603a0

Bonjean, V., Aghanim, N., Salomé, P., Douspis, M., & Beelen, A. 2018, A&A, 609, A49, doi: 10.1051/0004-6361/201731699

Cautun, M., van de Weygaert, R., Jones, B. J. T., & Frenk, C. S. 2014, MNRAS, 441, 2923, doi: 10.1093/mnras/stu768

Clampitt, J., Miyatake, H., Jain, B., & Takada, M. 2016, MNRAS, 457, 2391, doi: 10.1093/mnras/stw142

Colberg, J. M., Krughoff, K. S., & Connolly, A. J. 2005, MNRAS, 359, 272, doi: 10.1111/j.1365-2966.2005.08897.x

Colless, M., Dalton, G., Maddox, S., et al. 2001, MNRAS, 328, 1039, doi: 10.1046/j.1365-8711.2001.04902.x

DESI Collaboration, Abdul-Karim, M., Adame, A. G., et al. 2025, arXiv e-prints, arXiv:2503.14745, doi: 10.48550/arXiv.2503.14745

Dietrich, J. P., Werner, N., Clowe, D., et al. 2012, Nature, 487, 202, doi: 10.1038/nature11224

Dolag, K., Meneghetti, M., Moscardini, L., Rasia, E., & Bonaldi, A. 2006, MNRAS, 370, 656, doi: 10.1111/j.1365-2966.2006.10511.x

Epps, S. D., & Hudson, M. J. 2017, MNRAS, 468, 2605, doi: 10.1093/mnras/stx517

Flaugher, B., Diehl, H. T., Honscheid, K., et al. 2015, AJ, 150, 150, doi: 10.1088/0004-6256/150/5/150

Foreman-Mackey, D. 2016, The Journal of Open Source Software, 1, 24, doi: 10.21105/joss.00024

Foreman-Mackey, D., Hogg, D. W., Lang, D., & Goodman, J. 2013, PASP, 125, 306, doi: 10.1086/670067

Fu, S., Dell'Antonio, I., Chary, R.-R., et al. 2022, ApJ, 933, 84, doi: 10.3847/1538-4357/ac68e8

Fu, S., Dell'Antonio, I., Escalante, Z., et al. 2024, ApJ, 974, 69, doi: 10.3847/1538-4357/ad67c6

Haines, C. P., Busarello, G., Merluzzi, P., et al. 2018, MNRAS, 481, 1055, doi: 10.1093/mnras/sty2338

Harris, C. R., Millman, K. J., van der Walt, S. J., et al. 2020, Nature, 585, 357, doi: 10.1038/s41586-020-2649-2

Helou, G., Madore, B. F., Schmitz, M., et al. 1991, in Astrophysics and Space Science Library, Vol. 171, Databases and On-line Data in Astronomy, ed. M. A. Albrecht & D. Egret, 89–106, doi: 10.1007/978-94-011-3250-3_10

Higuchi, Y., Oguri, M., & Shirasaki, M. 2014, MNRAS, 441, 745, doi: 10.1093/mnras/stu583

Higuchi, Y., Okabe, N., Merluzzi, P., et al. 2020, MNRAS, 497, 52, doi: 10.1093/mnras/staa1766

Hincks, A. D., Radiconi, F., Romero, C., et al. 2022, MNRAS, 510, 3335, doi: 10.1093/mnras/stab3391

Hirata, C., & Seljak, U. 2003, MNRAS, 343, 459, doi: 10.1046/j.1365-8711.2003.06683.x

Hoekstra, H. 2001, A&A, 370, 743, doi: 10.1051/0004-6361:20010293

Hunter, J. D. 2007, Computing in Science & Engineering, 9, 90, doi: 10.1109/MCSE.2007.55

HyeongHan, K., Jee, M. J., Cha, S., & Cho, H. 2024, Nature Astronomy, 8, 377, doi: 10.1038/s41550-023-02164-w

Jauzac, M., Jullo, E., Kneib, J.-P., et al. 2012, MNRAS, 426, 3369, doi: 10.1111/j.1365-2966.2012.21966.x

Jones, D. H., Read, M. A., Saunders, W., et al. 2009, MNRAS, 399, 683, doi: 10.1111/j.1365-2966.2009.15338.x

Kondo, H., Miyatake, H., Shirasaki, M., Sugiyama, N., & Nishizawa, A. J. 2020, MNRAS, 495, 3695, doi: 10.1093/mnras/staa1390

Kull, A., & Böhringer, H. 1999, A&A, 341, 23, doi: 10.48550/arXiv.astro-ph/9812319

M. Schirmer. 2004, PhD thesis, Rheinische Friedrich-Wilhelms-Universität Bonn. https://hdl.handle.net/20.500.11811/2017

Mandelbaum, R., Hirata, C. M., Seljak, U., et al. 2005, MNRAS, 361, 1287, doi: 10.1111/j.1365-2966.2005.09282.x

Mandelbaum, R., Miyatake, H., Hamana, T., et al. 2018, PASJ, 70, S25, doi: 10.1093/pasj/psx130

Marinacci, F., Vogelsberger, M., Pakmor, R., et al. 2018, MNRAS, 480, 5113, doi: 10.1093/mnras/sty2206

Maturi, M., Angrick, C., Pace, F., & Bartelmann, M. 2010, A&A, 519, A23, doi: 10.1051/0004-6361/200912866

Maturi, M., Meneghetti, M., Bartelmann, M., Dolag, K., & Moscardini, L. 2005, A&A, 442, 851, doi: 10.1051/0004-6361:20042600

Maturi, M., & Merten, J. 2013, A&A, 559, A112, doi: 10.1051/0004-6361/201322007

McCleary, J., dell'Antonio, I., & von der Linden, A. 2020, ApJ, 893, 8, doi: 10.3847/1538-4357/ab7c58

Mead, J. M. G., King, L. J., & McCarthy, I. G. 2010, MNRAS, 401, 2257, doi: 10.1111/j.1365-2966.2009.15840.x

Merluzzi, P., Busarello, G., Haines, C. P., et al. 2015, MNRAS, 446, 803, doi: 10.1093/mnras/stu2085

Migkas, K., Pacaud, F., Tuominen, T., & Aghanim, N. 2025, A&A, 698, A270, doi: 10.1051/0004-6361/202554944

Mirakhor, M. S., Walker, S. A., & Runge, J. 2022, MNRAS, 509, 1109, doi: 10.1093/mnras/stab2979

Mitsuishi, I., Gupta, A., Yamasaki, N. Y., et al. 2012, PASJ, 64, 18, doi: 10.1093/pasj/64.1.18

Naiman, J. P., Pillepich, A., Springel, V., et al. 2018, MNRAS, 477, 1206, doi: 10.1093/mnras/sty618

NASA/IPAC Extragalactic Database (NED). 2019, IPAC, doi: 10.26132/NED1

Navarro, J. F., Frenk, C. S., & White, S. D. M. 1997, ApJ, 490, 493, doi: 10.1086/304888

Nelson, D., Pillepich, A., Springel, V., et al. 2018a, MNRAS, 475, 624, doi: 10.1093/mnras/stx3040

Nelson, D., Pillepich, A., Springel, V., et al. 2018b, MNRAS, 475, 624, doi: 10.1093/mnras/stx3040

Osato, K., Liu, J., & Haiman, Z. 2021, MNRAS, 502, 5593, doi: 10.1093/mnras/stab395

Paterno-Mahler, R., Blanton, E. L., Randall, S. W., & Clarke, T. E. 2013, ApJ, 773, 114, doi: 10.1088/0004-637X/773/2/114

Piffaretti, R., Arnaud, M., Pratt, G. W., Pointecouteau, E., & Melin, J. B. 2011, A&A, 534, A109, doi: 10.1051/0004-6361/201015377

Pillepich, A., Nelson, D., Hernquist, L., et al. 2018, MNRAS, 475, 648, doi: 10.1093/mnras/stx3112

Radiconi, F., Vacca, V., Battistelli, E., et al. 2022, MNRAS, 517, 5232, doi: 10.1093/mnras/stac3015

Rowe, B. T. P., Jarvis, M., Mandelbaum, R., et al. 2015, Astronomy and Computing, 10, 121, doi: 10.1016/j.ascom.2015.02.002

Shinde, R., Winkler, A., & Dell'Antonio, I. 2025, in American Astronomical Society Meeting Abstracts, Vol. 245, American Astronomical Society Meeting Abstracts #245, 472.03

Sohn, J., Geller, M. J., Walker, S. A., et al. 2019, ApJ, 871, 129, doi: 10.3847/1538-4357/aaf1cc

Springel, V., White, S. D. M., Jenkins, A., et al. 2005, Nature, 435, 629, doi: 10.1038/nature03597

The pandas development Team. 2025,, v2.3.1 Zenodo, doi: 10.5281/zenodo.3509134

Ursino, E., Galeazzi, M., Gupta, A., et al. 2015, ApJ, 806, 211, doi: 10.1088/0004-637X/806/2/211

Virtanen, P., Gommers, R., Oliphant, T. E., et al. 2020, Nature Methods, 17, 261, doi: 10.1038/s41592-019-0686-2

Walker, S. A., Fabian, A. C., Sanders, J. S., George, M. R., & Tawara, Y. 2012, MNRAS, 422, 3503, doi: 10.1111/j.1365-2966.2012.20860.x

Werner, N., Finoguenov, A., Kaastra, J. S., et al. 2008, A&A, 482, L29, doi: 10.1051/0004-6361:200809599

Wes McKinney. 2010, in Proceedings of the 9th Python in Science Conference, ed. Stéfan van der Walt & Jarrod Millman, 56 – 61, doi: 10.25080/Majora-92bf1922-00a

Xia, Q., Robertson, N., Heymans, C., et al. 2020, A&A, 633, A89, doi: 10.1051/0004-6361/201936678

Zehavi, I., Zheng, Z., Weinberg, D. H., et al. 2011, ApJ, 736, 59, doi: 10.1088/0004-637X/736/1/59